ANUL XLVIII **2003**

S T U D I A
UNIVERSITATIS BABEŞ-BOLYAI
PHYSICA
1

EDITORIAL OFFICE: Republicii no. 24, 400015 Cluj-Napoca ♦ Phone 0264-40.53.52

CONTENTS

STUDIA UNIVERSITATIS BABEŞ-BOLYAI, PHYSICA, XLVIII, 1, 2003

DEVELOPMENT OF SOLENOIDAL IMPLANTABLE DETECTION MICROCOILS FOR MINIMALLY INVASIVE NMR SPECTROSCOPY

M. ARMENEAN[12], L. BERRY[3], O. COZAR[1], H. SAINT-JALMES[2]

ABSTRACT. In this paper, we describe an implantable solenoidal microcoil of 200 μm in diameter for Nuclear Magnetic Resonance spectroscopy (NMR spectroscopy). This microcoil is used as receiving coil only during experiments. A simulation of the electromagnetic properties of this microcoil is proposed and compared to the experimental measurement. ^{1}H spectra of 0.33 cm^3 sample of a deionized water or of a lipid compound sample were taken at 2 T, using such solenoidal microcoil (85.13 MHz).

KEYWORDS: Minimally invasive NMR spectroscopy, Implantable microcoils, Solenoids

1. Introduction

Compared to other common spectroscopic methods of molecular characterisation, Nuclear Magnetic Resonance (NMR) is by far the least sensitive [1, 2]. NMR is seldom the method of choice for analysis of trace level quantities, despite its strong structural identification capability and non-destructive nature. Recently, much research has focused on the optimisation of the Radio-Frequency (RF) coils for the analysis of trace level quantities. Since sensitivity of NMR (RF) coil varies inversely with coil diameter, many authors have worked on the miniaturisation of the RF detection devices [2, 3, 4, 5]. In this way, two main approaches were studied.

The first approach consists in using solenoidal microcoils as flow probes for static and dynamic NMR measurements. Typically, those solenoidal microcoils are made using a long capillary to be filled with the observed liquid sample.

In the second approach, planar microcoils requires microelectronic fabrication technology. This fabrication process guarantees a good reproducibility and allows reduction of RF microcoil dimensions and its integration with electronic circuits. According to their structures, they could be used as implantable microcoil. Since NMR spectroscopy typically provides the most extensive chemical information, implantable microcoil could be useful for a selective detection of living metabolites tissues. However, even if the first results obtained on liquid sample are encouraging, improvements must be made to use them as implantable microcoils.

[1] *Babes-Bolyai University, Dept. of Physics, 1 Kogalniceanu, 3400 Cluj-Napoca, Romania*
[2] *Laboratoire de RMN, UMR CNRS 5012, Université Claude Bernard Lyon 1 ESCPE Lyon, 69622 Villeurbanne Cedex, France.*
[3] *LENAC JE 2266, Université Claude Bernard Lyon1– bât. 203, 69622 Villeurbanne Cedex, France.*

In this paper, we describe a new type of microcoil: an implantable NMR solenoidal microcoil. The outer diameter of the coil was approximately 200 μm and the length was 580 μm. The originality of this microcoil is that it was glued with an adhesive resin which allows its use as an implantable microcoil. This means the sample that must be analysed can't be put on the inside of the microcoil. The sample is on the outside, all around the microcoil. Electromagnetic characteristics of the microcoil evaluated by simulation are proposed in order to link the geometric parameters of the microcoil to the performances of the microcoil. The development of an accurate estimate of the signal-to-noise ratio (SNR) of these NMR microcoil as a function of its parameters is important in order to design microcoil with the highest possible SNR.

Experimental verifications are accomplished using the solenoidal microcoil in NMR spectroscopy experiments at 2 T (85.13 MHz).

2. Micro-fabrication steps of the microcoil

The solenoidal microcoil was made by wrapping wire around a silica capillary.The silica capillary was of 164 μm in outer diameter. At one extremity of the silica capillary, a copper tube of 220 μm in inner diameter was glued with cyanoacrylate adhesive to be used as a rigid coaxial cable. The wire was of 20 μm in diameter, 99.99% copper. After the introduction of the copper wire in the silica capillary, the copper wire was fixed at one extremity of the silica capillary with cyanoacrylate adhesive. Then the capillary was placed in a pine vise and the pine vise was rotated to start wrapping the coil. 15 turns were wrapped with a spacing between adjacent wires of 20 μm. The extremity of the copper wire was then soldered on the copper tube.

At the end, the extremity of the solenoidal microcoil was glued with an adhesive resin. In consequence, the solenoidal microcoil could now be used as an implantable microcoil (Fig. 1).

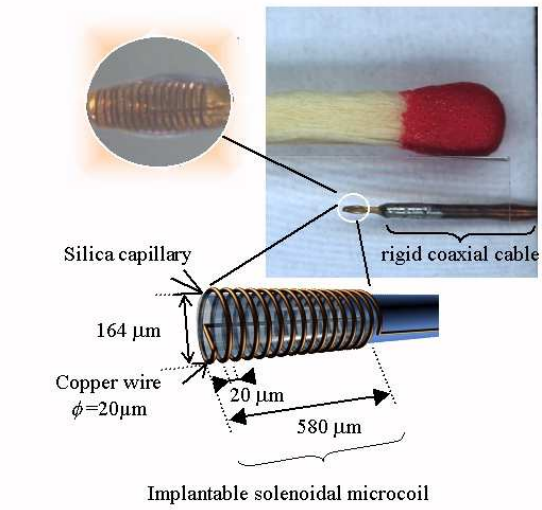

Fig. 1. Schematic representation of implantable solenoidal microcoil

3. The principles of proton NMR

The precession of the sample magnetisation M of nuclear origin around the static magnetic field Bo induces a current in the receiving coil. The axis of this receiving coil is perpendicular to Bo.

To enhance the detection selectivity of this movement, the circuit is tuned to the rotation frequency of the magnetisation M (the coil is so called resonator). Consequently, the characteristic of the NMR spectrum is directly linked to the quality of this resonator [6].

4. Simulation of the electromagnetic characteristics of the microcoil

Simulation of the electromagnetic fields and eddy current effects induced in the microcoil from sinusoidal current sources was done using the ANSOFT Maxwell 2D/3D software. Skin and proximity effects are also fully modelled. Maxwell 2D/3D is based on a finite element method, a widely used mathematical method optimal for solving a broad range of electromagnetic field problems. With the geometric characteristics of the microcoil, this simulation tool evaluate the electromagnetic characteristics (R, L, B) of the microcoil. The Signal–to-Noise Ratio (SNR) of an NMR experiment is defined as the peak signal divided by the root mean square (rms) noise [7]:

$$SNR = \frac{\frac{B_1}{i} V_S N\gamma \frac{h^2}{4\pi^2} I(I+1) \frac{\omega_0^2}{3\sqrt{2}kT}}{V_{noise}}$$

with

$$V_{noise} = \sqrt{4k\,TR_{noise}\,\Delta f}$$

where B_1/i is the magnetic field per unit current (coil sensitivity), V_S the sample volume, N the spin density, γ the gyromagnetic ratio, I the spin quantum number, ω_0 the nuclear precession frequency, T the sample temperature, k the Boltzmann's constant, h the Planck's constant and Δf is the spectral bandwidth.

At reduced dimensions of the sample, the noise originating within the sample is negligible when compared to the noise of the coil [8]. In this condition, the noise due to the sample resistance is usually small compared to the noise due to the microcoil resistance ($R_{noise} \approx R_{coil}$). The resistance of a wire increases with frequency. The current is concentrated towards the outer edge of the conductor (skin effect), with the current density decreasing exponentially from the wire surface to the centre. The second factor to be considered in the current distribution is the proximity effect. The magnetic field lines from a given turn of a solenoidal coil induce eddy currents in adjacent turns, further distorting the current distribution and increasing the resistance of coil [9] (Fig. 2). For f = 85.13 MHz (corresponding to the proton resonance frequency at 2 T), inductance and resistance of the microcoil were estimated respectively at 10.5 nH and 0.635 Ω. The value of the quality factor Q was calculated to be 8.87.

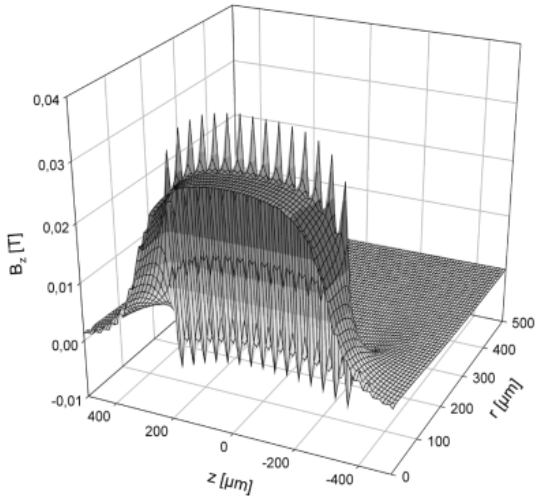

Fig. 2. The axial component of magnetic field for the solenoidal microcoil for I = 1 A

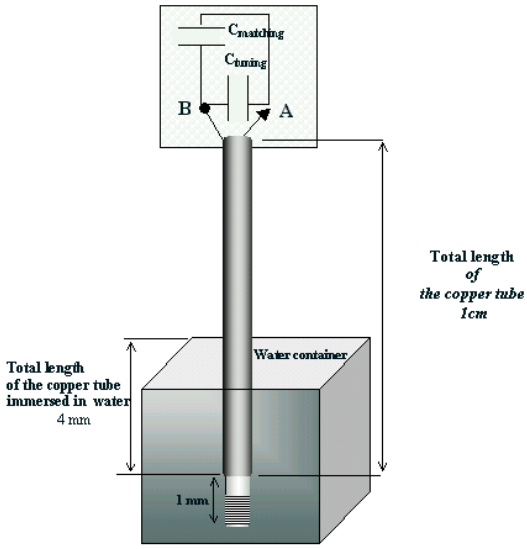

Taking in to account the coaxial cable attached to the coil (R= 0.726 Ω, L = 4.78 nH), the resulting Q factor is 6. The SNR computation made for proton in water at 2 T (f = 85.13 MHz), T = 37 °C and Δf/f = 6 ppm, is 110 assuming the solenoidal microcoil and 4 mm of the rigid coaxial cable are immersed in water (Fig. 3).

Fig. 3. Experimental conditions

5. Experimental verification

5. 1. Electromagnetic characterisation

We have used a conventional tuning-matching circuit to optimise the NMR signal transmission through the rigid coaxial cable (Fig. 4). Using a network analyser 4195A (Hewlett Packard), the coil was tuned to a frequency of 85.13 MHz (C_{tuning}) and matched at 50 Ω for this frequency ($C_{matching}$).

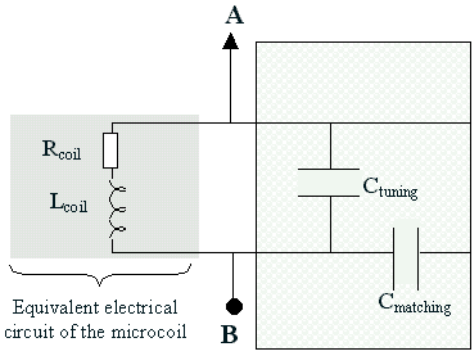

Electromagnetic characterisation of the microcoil was performed. The value of the quality factor Q was measured to be 5.1 at 85.13 MHz. The value of the quality factor measured in the experiment is in good agreement with the one evaluated by simulation.

Fig. 4. Circuit for tuning and matching

5.2 NMR measurements

We have realised two NMR measurements: the first in 0.33 cm^3 of a deionized water sample and the second in 0.33 cm^3 of a lipid compound sample (butter). In the NMR experiments, while a large RF coil surrounding the sample was used for the excitation, the implantable solenoidal microcoil was only used to receive the signal.

In the first experiment, the implantable solenoidal microcoil was immersed in a small deionized water sample (0.33 cm^3) to obtain the Proton spectrum of the water. Fig. 5 represents the Free Induction Decay of signal (FID) corresponding to the Proton which was acquired at 2 T with 4 averages corresponding to a scan time of 6 seconds. Fig. 6 shows the corresponding Proton spectrum. The quality of the Proton spectrum demonstrates the Signal-to-Noise Ratio is correct; a SNR of 84 was experimentally estimated.

A second experiment was realised to have a better evaluation of the spectral resolution. The implantable solenoidal microcoil was immersed in a lipid compound sample (0.33 cm^3). Proton spectrum was acquired at 2 T with 6 averages corresponding to a scan time of 9 seconds. The resolution in frequency of the microcoil allowed us to distinguish water group from (CH_2-CH_3) fat group on the ^1H spectra (Fig. 7). The difference in frequency was 298 Hz, which corresponds to 3.5 ppm. In conclusion, the implantable solenoidal microcoil NMR has been successfully tested for ^1H NMR at 85.13 MHz.

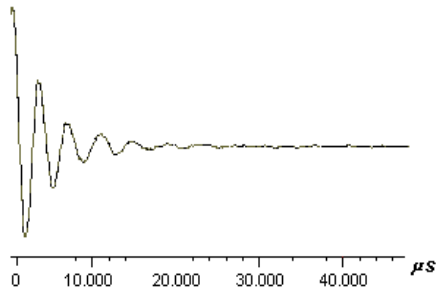

Fig. 5. NMR FID of a deionized water sample acquired at 2T during 6 sec after filtering.

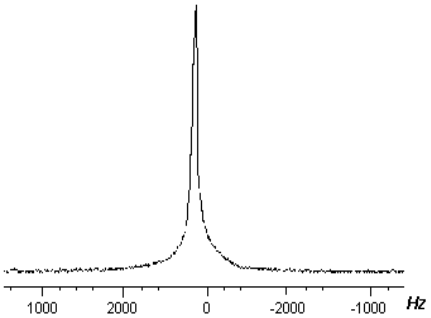

Fig. 6. ^1H spectra of a deionized water sample acquired at 2T during 6 sec after filtering.

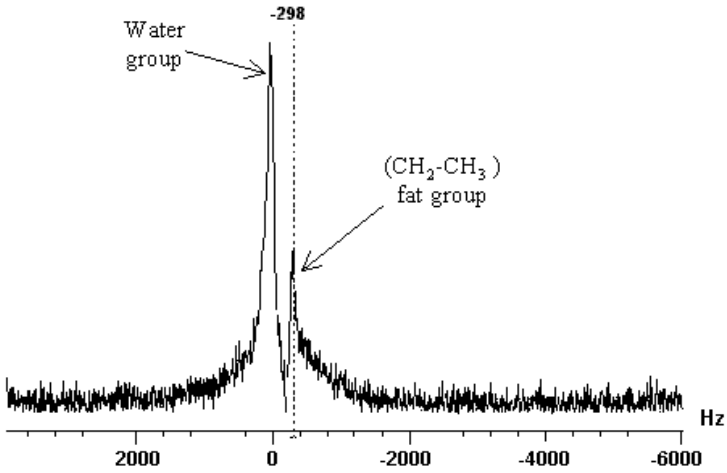

Fig. 7a. ^{1}H spectra of a lipid compound sample acquired at 2T during 9 sec without filter.

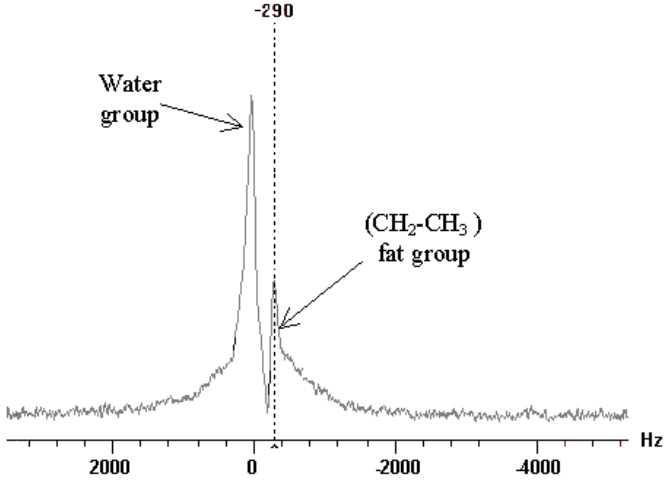

Fig. 7b. ^{1}H spectra of a lipid compound sample acquired at 2T during 9 sec with filter.

6. Conclusion and perspectives

In this study, we have shown a good correlation between the quality factor Q of the microcoil obtained by simulation and measured during the experiment. Simulation of the electromagnetic characteristics (R, L, B) of the microcoil was done using the ANSOFT Maxwell 2D/3D software which is an useful mean to optimise the electromagnetic performances of microcoils.

Those first results obtained with the implantable solenoidal microcoil have validated the miniaturisation of the NMR experiment and they represent a significant advanced for in-vivo NMR spectroscopy.

For the next step, the implantable microcoil will be used to follow the brain energy variation during the paradoxical sleep of a rat. The understanding of the paradoxical sleep can be enriched by the measurement of ATP metabolites during this state [10]. In this way, the implantable microcoil will be tuned and matched to detect ^{31}P of ATP metabolites presents in cerebral tissues during paradoxical sleep. This minimally invasive NMR spectroscopy means to reduce the dimensions of the microcoil in order to maintain a good quality of sleep states. In this way, the main challenge will consist in optimising the Signal–to-Noise Ratio.

An other perspective is to develop planar microcoils optimised with the help of an electromagnetic simulation software and realised with microelectronic fabrication technology*.*

Acknowledgements

We acknowledge the assistance and technical support of Linda Chaabane (Laboratoire RMN).

REFERENCES

1. C.L.Putzig, M.A. Leugers, M.L. McKelvy, G.E. Mitchell, R.A. Nyquist, R.R. Papenfuss, L. Yurga, Anal. Chem., 26R, 66 (1994).
2. Dean L. Olson, Timothy L. Peck, Andrew G. Webb, Richard L. Magin, and Jonathan V. Sweedler, Science, 270, 1967 (1995).
3. R. Subramanian, M.M. Lam and A.G. Webb, 133, 227 (1998).
4. R. L. Magin, A. G. Webb and T. L. Peck, IEEE spectrum, 34, 51 (1997).
5. G. Boero, C. de Raad Iseli, P.A. Besse, R.S. Popovic, Sensors and Actuators A67, 18 (1998).
6. A. Abragam, The principles of nuclear magnetism, Oxford University Press, 1961.
7. D.I. Hoult, Journal of Magnetic Resonance 24, 71 (1976).
8. T.L. Peck, R.L. Magin, P.C. Lauterbur, Journal of Magnetic Resonance, B108, 115 (1995).
9. A.G. Webb, Progress in NMR Spectroscopy, 31, 14 (1997).
10. R. Cespuglio, Rev. Neurol., 156/3, 320 (2000).

STUDIA UNIVERSITATIS BABEŞ-BOLYAI, PHYSICA, XLVIII, 1, 2003

THE SPIN FLUCTUATIONS IN THE $UNi_{5-Z}Al_Z$ SYSTEMS

ILEANA LUPSA, P. LUCACI[1]

ABSTRACT. The magnetic properties of $U_{1-X}Dy_XNi_5$ and $U_{1-x}Dy_xAlNi_4$ systems were investigated in the 4-600 K temperature range and fields up to 9 T. The UNi_5 and $UAlNi_4$ compounds show an enhanced susceptibility below 140 K and a Pauli paramagnet behaviour in the high temperature region. The compounds $DyNi_5$ and $DyNi_4Al$ are magnetically ordered below the transition temperatures 11.5 K and 8 K respectively. A Ni magnetic moment is detected for $DyNi_5$ and a small one for $DyNi_4Al$. In the high temperature region an effective magnetic moment per nickel atom is evidenced. Replacing uranium by dysprosium these μ_{eff}/Ni atom values are decreasing. The paramagnetic Curie temperatures for $x \geq 0.8$ are negative and are decreasing as uranium content is increased. The magnetic behaviour of Ni atoms was discussed in the spin fluctuations model.

Introduction

The aim of this paper is to study the presence of the spin fluctuations associated to Ni atoms in the systems starting from the compounds $UNi_{5-Z}Al_Z$ with z=0 and 1 where U is gradually substituted by a magnetic rare earth (dysprosium) [1,2].

The compounds UNi_5 and UNi_4Al have a cubic crystalline structure of $AuBe_5$ type with the lattice constant of 0.685 nm and 0.681 nm respectively [2,3]. The compounds show in the high temperature region a Pauli paramagnetism and in the low temperature region an enhanced susceptibility[4].

The magnetically ordered heads of this serie $DyNi_5$ and $DyNi_4Al$ have a hexagonal structure of $CaCu_5$ type with lattice parameters a=0.4882 nm and c=0.3951 nm for z=0 and a=0.4928nm and c=0.4038nm for z=1.

Experimental details

The investigated systems where obtained from 3N purity for uranium and better for the other elements. These were melted from the stoichiometric amounts of elements in an arc furnace in a purified argon atmosphere. The thermal treatment under vacuum during one week at 1000 K was performed.

The standard X-ray diffraction method in order to determine the structural phases and lattice parameters was used. In $U_{1-X}Dy_XNi_5$ for x=0.8 and in $U_{1-X}Dy_XNi_4Al$ for x=0.6 a mixture of two types of cubic and hexagonal phases is present. The magnetic measurement were carried out in the 1.7(5)-600K temperature range and fields up to 9T. The spontaneous magnetization M_0 were obtained from the magnetization isotherms according to the approach to saturation law: $M=M_0(1- b/H)$ where b represents the coefficient of the magnetic hardness.

In the paramagnetic range the susceptibility values were calculated from their field dependence according to Honda-Owen rule: $X_{m=}X_{+}cM_s^{'}H^{-1}$. Extrapolating

[1] *Technical University, 3400 Cluj – Napoca, Romania*

to $H^{-1} \rightarrow 0$, the correct X values are obtained. χ_m is the measured susceptibility, c represents the presumed impurity concentration and M_S' is its saturation magnetization. The influence on X of the possible magnetically ordered impurity is in this way eliminated.

Results

The magnetic investigations show that UNi_5 and $UAlNi_4$ are exchange enhancement paramagnets. For UNi_5 a maximum in the susceptibility in the low temperature region is evidenced. In the high temperature region the compounds display a constant susceptibility (Fig.1).

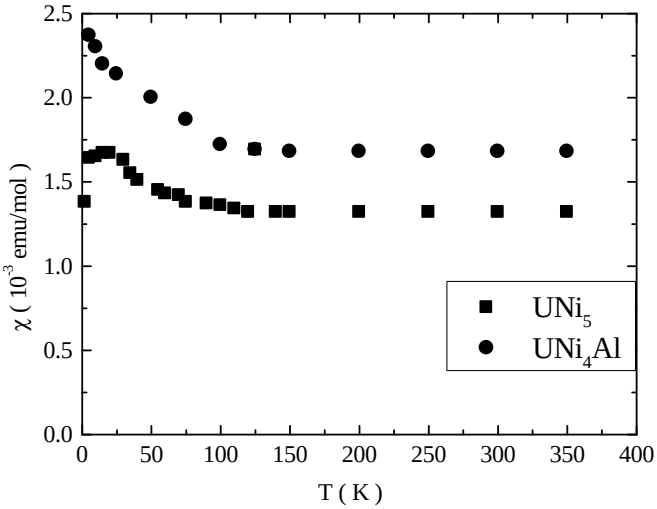

Fig. 1. The thermal dependences of the susceptibility for $DyNi_5$ and $DyAlNi_4$

For the systems $DyNi_5$ and $DyNi_4Al$ the ordered state below 11.5 K and 8 K respectively is present. The magnetizations values for $U_{1-X}Dy_XNi_5$ are lower then the values expected for Dy^{3+} supporting a magnetic moment for Ni ions.The value of magnetic moment per Ni atom is decreasing as Dy content diminishes from 0.25 μ_B/Ni atom. The saturation magnetization of $U_{1-X}Dy_XAlNi_4$ systems has the same values as Dy^{3+} ions for $x>0.4$ and lower values for $0.2 \leq x \leq 0.4$. For these two samples an linear increasing in the field magnetization dependence is present even up to 9T indicating incomplete saturation.

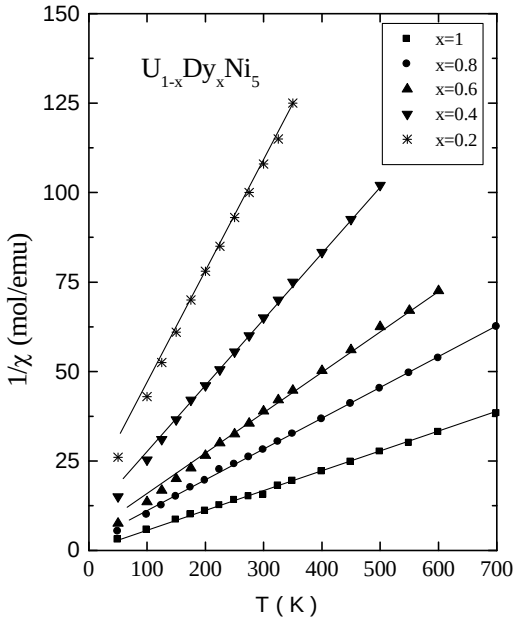

Fig. 2a. The thermal variation of the reciprocal susceptibility for $U_{1-X}Dy_XNi_5$ systems

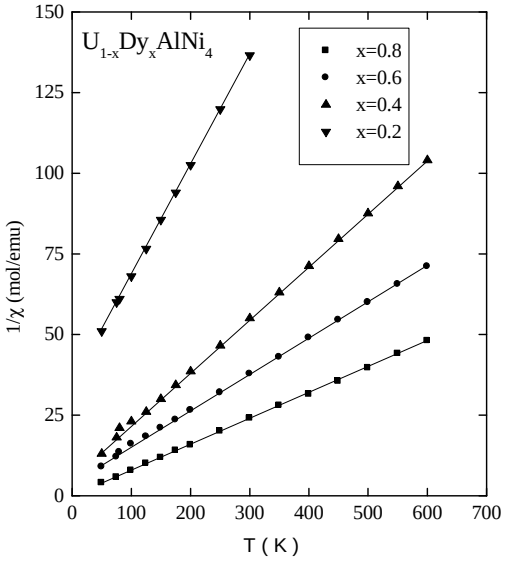

Fig.2b. The thermal variation of the reciprocal susceptibility for $U_{1-x}Dy_xAlNi_4$ systems

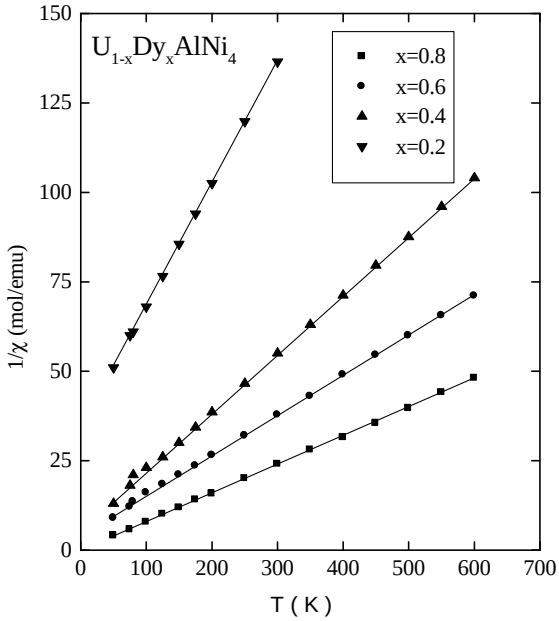

Fig. 3. The composition dependence of the molar Curie constant and the paramagnetic Curie temperature for $U_{1-X}Dy_XNi_5$ and $U_{1-x}Dy_xAlNi_4$

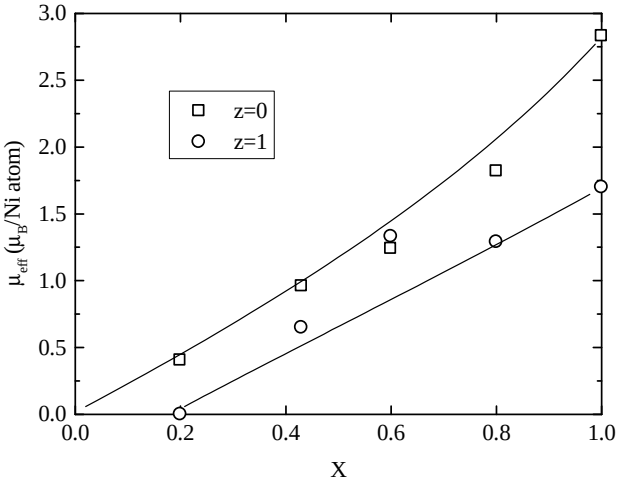

Fig .4.The composition dependence of the effective magnetic moment per Ni atom for $U_{1-X}Dy_XNi_5$ and $U_{1-x}Dy_xAlNi_4$

In the paramagnetic range the thermal dependence of the reciprocal susceptibility indicate the typical ferrimagnetic behaviour for $U_{1-X}Dy_XNi_5$. The high temperature results lead to the paramagnetic Curie temperatures and the molar Curie constants shown in Fig.2a. For $U_{1-X}Dy_XAlNi_4$ systems the Curie-Weiss type paramagnetism is observed: $\chi = \frac{C}{T-\theta}$ (Fig.2b). The θ values become negative for x ~0.6, as it is shown in Fig.2. C values in the both systems are higher that the values corresponding to Dy^{3+} indicating the presence of the Ni ions contributions. These values are 18.18 emu K /mol and 16.04 emu K /mol respectively (Fig.3.). Assuming the superposition of Dy and Ni contribution in the magnetic properties we obtained the nickel influence on C values and μ_{eff}/Ni atoms. These values are higher in $U_{1-X}Dy_XNi_5$ system that in $U_{1-X}Dy_XAlNi_4$. For $DyNi_5$ the effective nickel magnetic moment is 2.83 μ_B that corresponding to Ni^{+2} state. The μ_{eff}/Ni atom are decreasing as Dy content becomes lower (Fig.4).

Discussion

The systems $DyNi_5$ and $DyAlNi_4$ are magnetically ordered below 11.5K and 8K respectively. A magnetic moment per Ni atom opposite orientated to Dy moment is present [5]. This moment is 0.25 μ_B/Ni for $DyNi_5$ and has a very low value for $DyAlNi_4$.

The gradual replacing of U with Dy leads to the decreasing of the magnetization value more than that corresponding to Dy^{3+} supporting the existence of a magnetic moment on Ni site. These values decrease as Dy content is decreasing. The Ni magnetic moment is very low for the system $U_{1-X}Dy_XAlNi_4$ and the magnetic moment values are mainly due to Dy^{3+} ions. In the low Dy concentration range $x \leq 0.4$, the magnetization becomes lower than that expected for Dy^{3+}. This behaviour is connected with the fact that the magnetization for these samples is not fully saturated and the θ values are negative. This supports the presence of a mictomagnetic type of order.

The low transition temperature of the systems are explained assuming that the exchange interactions Dy-Dy are less intense than that characteristic in Dy compounds of RKKY type [5]. As is reported for $DyNi_5$ compound [4] the interactions between Ni and Dy are more important that those between Ni ions; the Ni moments are determined by Dy ions. In $DyAlNi_4$, substituting an Al atom for a Ni one leads to the hybridization of Ni-3d and Al-3p bands and the decreasing the Ni moment very close to zero. In the paramagnetic region the effective magnetic moment per Ni is 1.69 μ_B lower than 2.83 μ_B the value in $DyNi_5$. The U substitution for Dy determines the decreasing of μ_{eff}/Ni almost in a linear manner. For $U_{1-X}Dy_XAlNi_4$ this decreasing is more intense that in the $U_{1-X}Dy_XNi_5$ systems. The systems UNi_5 and $UAlNi_4$ are exchange enhancement paramagnets showing a constant susceptibility over 110K.

The Ni atom behaviour in this system may be discussed in the selfconsistent SCR theory of the spin fluctuations [6,7,8] where the electron-electron correlations in the d band are considered.

For these weak or nearly ordered systems or strong exchange enhancement paramagnet, the dynamical susceptibility χ_q has increasing values for small wave number q and is significantly temperature dependent. The amplitude of the local spin fluctuations increases with temperature until it reaches an upper limit determined by the charge neutrality conditions and saturates at a certain temperature T*, above which the susceptibility is governed by local moment-type spin fluctuations and therefore a Curie-Weiss behaviour is observed. In the $U_{1-x}Dy_xAlNi_4$ system the transverse spin fluctuations due to Ni atoms are not saturated, the μ_{eff}/Ni_{atom} being lower than $2.83\mu_B$ the value expected for Ni^{+2} ion and found in $DyNi_5$. Substituting a Ni atom by Al determines a diminution of the electron correlations and the decreasing of the exchange enhancement factor.

REFERENCES

1. Z. Blazina and Z. Bem, J. Less. Common. Metals 33 (1973) 321

2 P. Villars and L. D. Calvert, Pearson's Handbook of Crystallographic Data for Intermetallic Phases, 1991

3. T. Takeshita, S. Malik and W. E. Wallace, Journal of Solid State Chemistry,23 (1978) 271

4. P. Lucaci, I. Lupsa and E. Burzo, Acta Physica Polonica A, 90 (1996) 565

5. E. Burzo, S. G. Chiuzbaian, M. Neumann, M. Valeanu, L. Chioncel and I. Creanga, J. Appl. Phys. 92 (2002), in press

6. T. Moriya, J. Magn. Magn. Mater.,14 (1979) 1

7. T. Moriya, J. Magn. Magn. Mater.,100 (1991) 20

8. K. Ikeda, K. A. Gschneidner Jr., R. J. Stierman, T. W. E. Tsang and O. D. McMasters, Phys. Rev.]\B, 29 (1984) 50

STUDIA UNIVERSITATIS BABEŞ-BOLYAI, PHYSICA, XLVIII, 1, 2003

HOMOGENEOUS ABSORPTION CROSS SECTION OF LEAD-BISMUTHATE GLASSES

R. POP[1], N. N. PUŞCAŞ[2], V. SIMON[3]

ABSTRACT. Results concerning transparence in infrared range of $xFe_2O_3(100-x)[3Bi_2O_3 \cdot 2PbO]$ glasses ($0 \le x \le 20$ mol %) are reported. The homogeneous absorption cross section was determined from optical absorption spectra using the density matrix formalism of McCumber theoretical model. The glass transition temperature with increasing Fe_2O_3 content was also investigated.

Introduction

Heavy metal glasses have attracted considerable attention due to their interesting physical properties such as high density, high polarisability, long infrared cut-off or high non-linear optical susceptibility leading to different applications like radiation shielding windows, scintillation counters, optical transmission devices, ultrafast optical switches [1-4]. Bismuth based glass systems can be converted into high-T_c superconductors after appropriate annealing [5]. An attractive reason in studying these glasses also consists in the fact that they do not contain any conventional glass formers such as SiO_2, B_2O_3, P_2O_5, GeO_2, etc.

For optical application the homogeneous absorption cross section of the lead-bismuthate glasses are needed in the modelling of the optical devices. The cross sections evaluated directly from experience are inhomogeneous because of glass structure disorder or of defects, dislocations, etc. occurring in crystalline samples, that lead to site-to-site variations of the surrounding field changing the energy positions of the Stark sublevels and also the dipole transition characteristics. There are several models used for the calculation of homogeneous absorption cross section [6, 7]. In this paper is investigated the effect of iron addition to $3Bi_2O_3 \cdot 2PbO$ glass matrix on glass transition temperature and on the transmission properties in infrared range of lead bismuthate glass samples containing iron.

Experimental

The starting materials used to prepare the samples were analytically pure reagents $(BiO)_2CO_3$, PbO and Fe_2O_3. The suitable mixtures were melted in

[1] *Physics Department, University of Civil Engineering, Bucharest, Romania*
[2] *Physics Department, Politehnica University, Bucharest, Romania*
[3] *Faculty of Physics, Babes-Bolyai University, 3400 Cluj-Napoca, Romania*
**Corresponding author. E-mail: viosimon@phys.ubbcluj.ro*

sintercorundum crucibles in an electric furnace, in air, at 1100 ^{0}C for 10 minutes. The melts were subsequently quenched between two stainless steel plates at room temperature. Differential thermal analysis (DTA) was carried out using a MOM-type thermal analyser. The DTA curves were recorded from powder samples, with a rate of 10^{o}C/min.

The absorption spectra were recorded in the spectral range 500 – 1100 nm by means of a standard Acton Research spectroscopic system with an R955 Hamamatsu photomultiplier. The experimental spectra were subsequently corrected for the spectral profiles of both the photomultiplier and the diffraction grating.

Results and discussion

The data obtained from differential thermal analysis curves regarding the glass transition temperature, T_g, are shown in Figure 1. One remarks an approximatively linear increase of glass transition temperature with Fe_2O_3 concentration, denoting that the structure of the glass sample becomes more rigid [8]. This result is in agreement with the observed structural effect of the alkali oxide addition to a lead-bismuthate matrix [9].

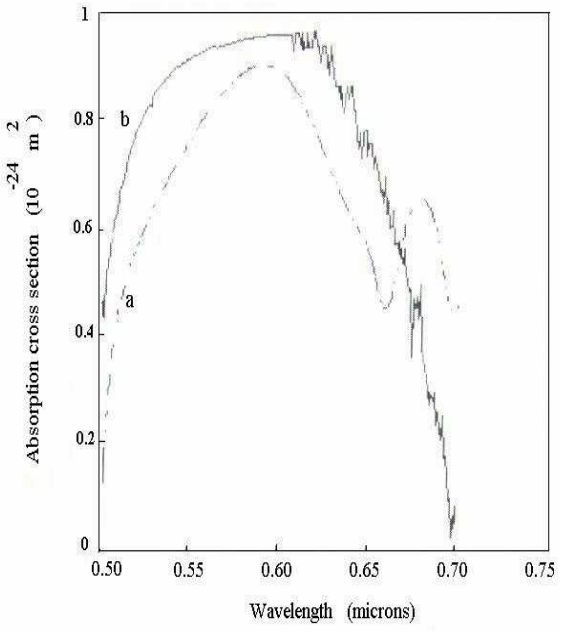

Fig. 1. Composition dependence of glass transition temperature for $xFe_2O_3(100-x)[3Bi_2O_3{\cdot}2PbO]$ samples.

Absorption spectra in visible and near infrared range were recorded from all samples in order to verify the transparence properties especially in infrared range. Figure 2 illustrates typical absorption spectra for the investigated glass system. One remarks a very good IR transmittane for the sample containing 10 mol % Fe_2O_3. This property is not observed neither for lower nor for higher Fe_2O_3 content. The valence state of the iron ions in this sample is preponderant Fe^{2+}, as evidenced from magnetic and EPR measurements [10, 11].

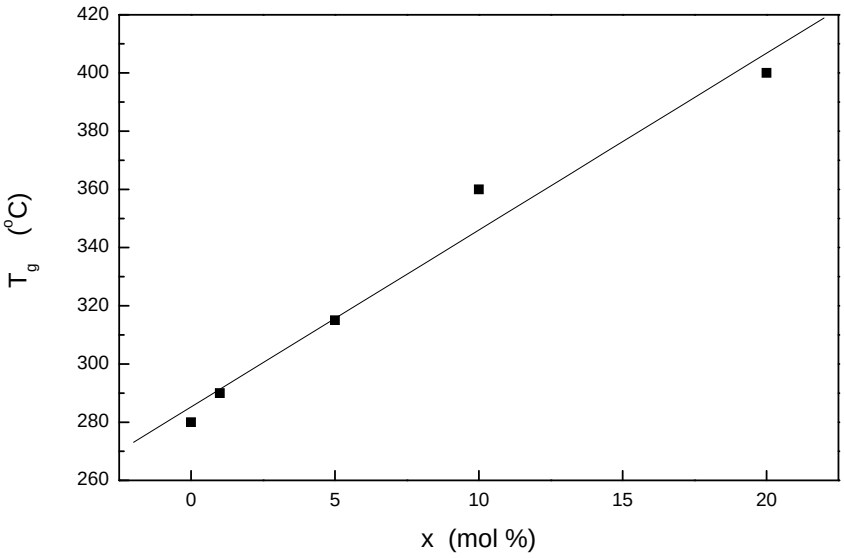

Fig. 2. Optical absorption spectra for some $xFe_2O_3(100-x)[3Bi_2O_3 \cdot 2PbO]$ glasses.

The absorption cross section $+_a$ is the ratio between the energy absorbed by an atom and the incident energy on surface unit an can be expressed as:

$$+_a = \frac{j}{NI} \cdot \frac{dI}{dz} = \frac{\gamma}{N} \quad (1)$$

where I is the intensity of the incident radiation, N is the density of atoms characterised by two energy levels and γ is the attenuation coefficient.

The Fuchtbauer-Ladenburg relation [6] can be used in order to evaluate the absorption cross sections from experimental data only in the case when the populations of the atomic Stark splitting sublevels are nearly equal, i.e. when the Stark splitting energy satisfies the condition $E < k_B T$. This is not the case in oxide glasses. Therefore we used the density matrix formalism for the the cross section computation [6, 7].

In order to evaluate the homogeneous cross sections and to describe the interaction between the atomic system and the electric field $E(z,t)$, we consider a Stark split two-level system and use the semiclassical formalism. The Heisenberg motion equation for the density matrix operator in this case is [6, 7]:

$$\frac{d\tilde{\rho}_{11}}{dt} = \frac{i}{\hbar} E(z,t) \sum_{j,k} \mu_{k,j} \left(\rho_{kj} - \rho_{jk} \right) - R_{12} \tilde{\rho}_{11} + A_{21} \tilde{\rho}_{22} \qquad (2)$$

$$\frac{d\tilde{\rho}_{22}}{dt} = -\frac{i}{\hbar} E(z,t) \sum_{j,k} \mu_{k,j} \left(\rho_{kj} - \rho_{jk} \right) - A_{21} \tilde{\rho}_{22} \qquad (3)$$

$$\frac{d\tilde{\rho}_{jk}}{dt} = i\omega_{kj} \rho_{kj} - \frac{i}{\hbar} E(z,t) \sum_{j,k} \mu_{k,j} \left(p_{2k,} \tilde{\rho}_{22} - p_{1j} \tilde{\rho}_{11} \right) - \tilde{A}^{r}_{jk} \tilde{\rho}_{jk} \qquad (4)$$

where μ_{kj} represent the elements of the dipole operator, $\tilde{\rho}_{11} = \sum \rho_{jj}$ and $\tilde{\rho}_{22} = \sum \rho_{kk}$ are the probabilities of the occupation of the split levels 1 and 2, $\rho_{jj} = p_{1j} \tilde{\rho}_{11}, \rho_{kk} = p_{2k} \tilde{\rho}_{22}$, are the matrix elements corresponding to individual Stark sublevels. R_{12} and A_{12} define the overall excitation of the atoms between the energetic levels $|E_1\rangle \rightarrow |E_2\rangle$ and the spontaneous emission rates, respectively corresponding to the two-level system and $A^r_{jk} = \Delta\omega_{kj} / 2$ corresponds to the full linewidth at half maximum (FWHM) of the transition centred at the frequency ω_{kj} .

The homogeneous absorption and emission cross sections can be determined from the experimental inhomogeneous cross sections $\sigma^I_a(\lambda)$ through the inverse Fourier transform relation and its properties [6]:

$$\sigma_a^H(\omega) = \sum_k a_k^a \frac{\Delta\omega_k}{2\sqrt{2\log 2}} F^{-1}\left\{\exp\left[-\frac{\left(\Delta\omega_k^2 - \Delta\omega_{inh}^2\right)x^2}{16\log 2} - i\omega_k x\right]; \omega\right\} \quad (5)$$

where $\Delta\omega = 2\pi c\Delta\lambda_{inh}/\lambda^2$ is the inhomogeneous bandwidth and $\Delta\lambda_{inh}$ the inhomogeneous linewidth.

The argument in the exponential function in Eq. (5) can be expressed as $b^2 - (ax-b)^2$, where the constants a and b are given by:

$$a = \frac{\Delta\omega_{inh}\sqrt{\beta_k^2 - 1}}{4\sqrt{\log 2}} \quad (6)$$

$$b = \frac{2\omega_k\sqrt{\log 2}}{\Delta\omega_{inh}\sqrt{\beta_k^2 - 1}} \quad (7)$$

where $\beta_k = \frac{\Delta\omega_k}{\Delta\omega_{inh}}$. Considering that $\beta_k > 1$, or $\Delta\omega_k > \Delta\omega_{inh}$ and using the translation property of Fourier transforms:

$$F^{-1}\left\{\exp\left[-(ax-b)^2; \omega\right]\right\} = \exp\left(-i\frac{b\omega}{a}\right)F^{-1}\left[\exp\left(-a^2x^2\right), \omega\right] \quad (8)$$

and the inverse relation

$$F^{-1}\left[\exp\left(-a^2x^2\right), \omega\right] = \frac{1}{a\sqrt{2}}\exp\left(-\frac{\omega^2}{4a^2}\right). \quad (9)$$

Eq. (9) leads to:

$$\sigma_a^H(\omega) = \sum_k a_k^a \frac{\Delta\omega_k}{\sqrt{\Delta\omega_k^2 - \Delta\omega_{inh}^2}}\left\{\exp\left[-4\log 2\frac{(\omega-\omega_k)^2}{\Delta\omega_k^2 - \Delta\omega_{inh}^2}\right]\right\}. \quad (10)$$

or as a function of wavelength in the form:

$$\sigma_{a,e}^H(\lambda) = \sum_j a_j^{a,e} \frac{\Delta\lambda_j}{\sqrt{\Delta\lambda_j^2 - \Delta\lambda_{inh}^2}}\left\{\exp\left[-4\log 2\frac{(\lambda-\lambda_j)^2}{\Delta\lambda_j^2 - \Delta\lambda_{inh}^2}\right]\right\}. \quad (11)$$

Based on the above presented model we estimated the homogeneous absorption cross section and we obtained the maximum cross section value σ_a^H (590 nm) = $0.91\cdot10^{-24}$ m^2 at 590 nm for $3Bi_2O_3.2PbO$ sample (Fig. 3).

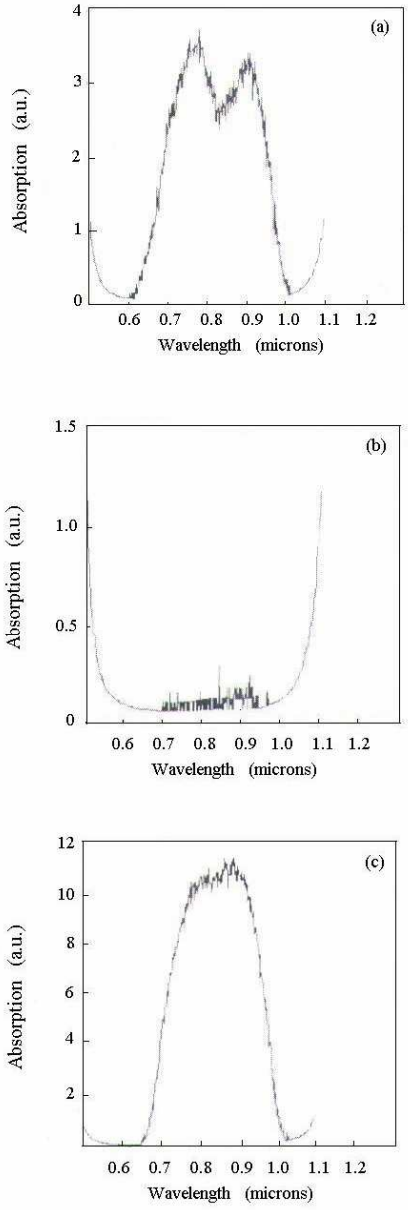

Fig. 3. The homogeneous (a) and inhomogeneous (b) cross sections for $3Bi_2O_3.2PbO$ glass matrix.

Conclusions

In $xF_2O_3(100-x)[3Bi_2O_3 \cdot 2PbO]$ glass system the iron oxide acts as network modifier and attracts by progressive addition the increase of the glass transition temperature. The homogeneous absorption cross section estimated using the density matrix formalism of McCumber model has a maximum value of $0.91 \cdot 10^{-24}$ m^2 around 600 nm for the lead-bismuthate glass matrix. The sample containing 10 mol % is highly transparent in the investigated spectral range.

REFERENCES

1. A. Karmalov, R. M. Almeida, and J. Heo, J. Non-Cryst. Solids, 202, pp. 233, 1996.
2. J. Fu, H. Yatsuda, Phys. Chem. Glasses, 36, pp. 211, 1995.
3. Y.B. Dimitriev, V.T. Mihailova, and J. Matter. Sci. Lett., 9, pp. 1251, 1990.
4. W.H. Dumbaugh, and J.C. Lapp, J. Am. Ceram. Soc., 75, pp. 2315, 1992.
5. T.Komatsu, R.Sato, K. Imai, K. Matusita, and T. Yamashita, Jap. Apll. Phys. 27, pp. 550, 1998.
6. E. Desurvire, Erbium-Doped Fiber Amplifiers, J. Wiley & Sons, Inc. New York/Chichester/Brisbane/Toronto/ Singapore, 1994.
7. N. N. Puscas, D. M. Grobnic, I. M. Popescu, M. Guidi, D. Scarano, G. Perrone, and I. Montrosset, Opt. Eng., 1685, pp. 1311, 1996.
8. V.Simon, R.Pop, S.Simon, Mod. Phys. Lett. B, 14, 29, 1025 (2000).
9. Pan , A.Gosh, J. Non-Cryst. Solids, 271, 157 (2000).
10. M.Coldea, V.Simon, N.N.Puscas, R.Pop, Rom. J. of Optoelectronics, 9, 2, 55 (2001).
11. S. Simon, R. Pop, V. Simon, M. Coldea (to be published).

STUDIA UNIVERSITATIS BABEŞ-BOLYAI, PHYSICA, XLVIII, 1, 2003

ANALYSIS OF $Y_{0.95}Bi_{0.05}Ba_2Cu_3O_x$ AND $Bi_2Sr_2Ca_{0.9}Gd_{0.1}Cu_2O_x$ SUPERCONDUCTING SAMPLES VIA ICP – OES TECHNIQUE

A. SIMON[1*]*, S.D. ANGHEL[1], T. FRENȚIU[2], M. PONTA[2], M.M. POP[3] AND S. SIMON[1]

ABSTRACT. The elemental content (concentrations and stoichiometric coefficients) of $Y_{0.95}Bi_{0.05}Ba_2Cu_3O_x$ and $Bi_2Sr_2Ca_{0.9}Gd_{0.1}Cu_2O_x$ superconducting samples was investigated via inductively coupled plasma source atomic emission spectroscopy technique. It was shown that plasma source atomic emission spectroscopy could be a very useful tool towards the quality control of superconducting materials preparation recepies or preparation technologies and could supply additional information about the supercondcuting samples. The results of our investigations are in good agreement with the AC susceptibility and XRD measurements.

1. Introduction

High-temperature superconducting materials are important components of several modern technologies. Establishing their elemental composition is a very important step for both sample preparation and practical applications, therefor characterization from this point of view requires highly accurate techniques for the determination of main components. According to the scientific literature [1–4], plasma source atomic emission spectroscopy proved to be a very suitable method for determination of stoichiometric composition of complex superconducting samples.

In this paper the elemental composition of superconducting oxides $Y_{0.95}Bi_{0.05}Ba_2Cu_3O_x$ and $Bi_2Sr_2Ca_{0.9}Gd_{0.1}Cu_2O_x$ was studied using inductively coupled plasma atomic emission spectroscopy (ICP-OES). The optimal operating conditions, line selections and detection limits are discribed for two ICP spectrometers, a secvential (SPECTROFLAME) and simultaneous one (SPECTRO CIROS ^{CCD}).

2. Experimental details

2.1 Superconducting sample preparation

Superconducting samples of $Y_{0.95}Bi_{0.05}Ba_2Cu_3O_x$ (123) and $Bi_2Sr_2Ca_{0.9}Gd_{0.1}Cu_2O_x$ (2212) were studied via ICP-OES technique. The superconducting sample preparation methods were discribed elsewhere [5].

[1] *"Babeş-Bolyai" University, Faculty of Physics, 3400 Cluj-Napoca, ROMANIA*
[*] *corresponding author, E-mail: asimon@phys.ubbcluj.ro*
[2] *"Babeş-Bolyai" University, Faculty of Chemistry, 3400 Cluj-Napoca, ROMANIA*
[3] *University of Amsterdam, Faculty of Science, Amsterdam, Holland*

The dissolving process of superconducting materials is the most important process towards elemental analysis, because the errors which may occure in this step will significantly affect the precision and the correctness of the analysis.

The superconducting samples were grinded in an agate mortar and sifted in a 60 μm sieve. From the resulted powder a quantity of 0.1 ± 0.0001 g sample was weighed and subject to further digestion in 0.5 M azotic acid at 80^{o}C. The cold mixtures were treated with H_2O_2 30% (puriss p.a. FLUKA) in order to eliminate any carbonic by-product and after that, heated again until the bubbling dissapeared. The cooled liquids were transferred into 100 mL volumetric flasks and diluted to the volume with HNO_3 2%. The azotic acid used for sample digestion (0.5 M), dilution (2 %) and as blank (2 %) was prepared from HNO_3 65% (puriss p.a. FLUKA). A further 20-fold sample dilution was used for the ICP-OES analysis of the 2212 type superconducting sample and a 40-fold one for the 123 type sample.

2.2 ICP-OES analysis

2.2.1 Reagents and standards

Single element stock solutions for ICP-OES, containing 1000 μg/mL of each metal, were prepared using analytical grade reagents (FLUKA). For calibration, eight multielement standards were prepared by the serial dilution of the stock solutions, in the following ranges: 0,4 - 40 μg/mL for Bi; 0,2 - 20 μg/mL for Sr; 0,05 - 5 μg/mL for Ca; 0,2 - 20 μg/mL for Cu; 0,1 - 12 μg/mL for Ba; 0,05 - 6 μg/mL for Y and 0,05 - 6 μg/mL for Gd.

2.2.2 Certified reference materials

In order to check the accuracy of elemental content determinations, a Bismuth-Strontium-Calcium-Copper-Oxide superconducting black powder (< 5 micron, from ALDRICH: Product no. 365106, CAS No. 114901-61-0), with the theoretical formula $Bi_2Sr_2Ca_1Cu_2O_{8+x}$ (x = 0.15 – 0.20) and ICP-OES certified elemental concentrations: Bi – 41 %, Sr – 20 %, Ca – 4.3 %, Cu – 13 %, was used as standard certified reference material (CRM).

2.2.3 Instrumentation

All analyses were performed using SPECTRO inductively coupled plasma atomic emission spectrometers. Details of instrumentation and operating conditions are listed in Table 1.

2.3 Accuracy and statistical validation

The accuracy tests and the statistical validations were performed according to Miller and Miller [6].

The accuracy of the elemental determinations by ICP-OES in the superconducting samples has been assessed by using a 2212-type superconducting CRM and the *t* – test according to:

$$t = \frac{(\bar{x} - \mu) \cdot \sqrt{n}}{s} \quad (1)$$

where s is the standard deviation, n is the number of parallel measurements, $\bar{x}$ is the average concentration determined for the CRM and μ is the certified concentration of a given element.

Table 1.

ICP instrumentation and operating conditions

ICP	SPECTROFLAME	SPECTRO CIROS^{CCD}
RF generator	• free-running type, at 27.12 MHz • variable power in the range of 750 – 1400 W (with no computer control) • P_{RF} = 1200 W	• free-running type, at 27.12 MHz • computer controlled variable power in the range of 750 – 1400 W (± 1 W) • P_{RF} = 1400 W
Plasma torch	• in vertical position (15 mm ALC) • Ar flow-rates: external 12 L/min; central 1L/min; nebulisation 1L/min	• in axial position • Ar flow-rates: external 12 L/min; central 1L/min; nebulisation 1L/min
Sample introduction	• 2 channel peristaltic pump (with computer controlled rotation speed) • sample flow-rate 2 mL/min • Meinhardt type concentric nebilizer • temperature controlled Scott type desolvatation chamber	• 4 channel peristaltic pump (with computer controlled rotation speed) • sample flow-rate 2 mL/min • cross-flow nebilizer • temperature controlled Scott type desolvatation chamber
Optics	• UV spectral range: 160 – 336 nm • diffraction grating: 3600 groves/mm • focal lenght: 750 mm • resolution: 15 pm • entrance slit: 15 μm • viewing through optical wire • VIS spectral range: 335 – 800 nm • diffraction grating: 2400 groves/mm • focal lenght: 750 mm • resolution: 15 pm • 8 entrance slits, each 10 μm wide • viewing through 8 optical wires, one for each entrance slit • 9781 R type photomultiplier tube oprated at 1000 V (Thorn EMI, Ruislip, Middlesex, Great Britain)	• Paschen – Runge mount • spectral range: 160 – 800 nm • focal length: 500 mm • primary grating: 2924 groves/mm • secondary grating: 2400 groves/mm • entrance slit: 10 μm • resolution: 9 pm/pixel. • array with 22 CCD type detectors (19 for UV and 3 for VIS)
Control and processing	• Smart Analyzer PC software (SPECTRO, Kleve, Germany)	

If the calculated value of *t*, for a probability P = 95 % and degree of freeweom ν = n – 1, is less than the value tabulated ([6], Appendix 2, Table A.1, p. 217) there are no significant differences between the results of the analysis and the certified values due to systematic errors. Thus, the ICP – OES technique would be a suitable method for the analysis of superconducting materials towards establishing the elemental composition.

If there are several parallel experimental determinations for each elemental concentration, with a given spectrometer, the values has to be statistically tested using the Dixon type *Q* – test in order to see if some of them were affected or not by systematic errors.

$$Q = \frac{|\text{the suspected value} - \text{the closest value}|}{\text{the highest value} - \text{the lowest value}} \tag{2}$$

If the calculated value of the Q coefficient is less then the tabulated one, Q_{tab}, $Q_{calc} < Q_{tab}$ (for P = 95 % and ν = n – 1, [6], Appendix 2, Table A.4, p.218), their average and the standard deviation could be calculated according to the following formulae:

$$\bar{x} = \frac{\sum_i x_i}{n} \tag{3}$$

$$s = \sqrt{\frac{\sum_i \left(x_i - \bar{x}\right)^2}{n-1}} \tag{4}$$

where $\bar{x}$, x_i, s and n represents the average concentration, an experimentally determined concentration, the standard deviation and the number of determinations during the analysis.

If the experimental determinations were performed with the same technique, but with two different equipments, obviously there will be two averages and two standard deviations. The standard deviation of the two averages, s_1 and s_2 are statistically compared using an *one-tailed F* – test:

$$F_{\nu_1,\nu_2} = \frac{s_1^2}{s_2^2} \tag{5}$$

ν_1 and ν_2 represents the degree of freedom for the two determination sets ($\nu_i = n_i - 1$, e.g. index *i* = 1 - ICP SPECTROFLAME, 2 - ICP SPECTRO CIROS^{CCD}).

The averages, $\bar{x}_1$ and $\bar{x}_2$, could be compared with the *t* – test according to the formula:

$$t = \frac{\bar{x}_1 - \bar{x}_2}{s\sqrt{\frac{1}{n_1} + \frac{1}{n_2}}} \tag{6}$$

$$\text{where: } s^2 = \frac{(n_1 - 1)s_1^2 + (n_2 - 1)s_2^2}{n_1 + n_2 - 2} \tag{7}$$

If $F_{calc} < F_{tab}$ (for P = 95 % and $\nu_1 = n_1 - 1$, $\nu_2 = n_2 - 1$, [6], Appendix 2, Table A.2, p.217) and $t_{calc} < t_{tab}$ (for P = 95 % and $n = n_1 + n_2 - 2$, [6], Appendix 2, Table A.1, p.217) there are no significant differences between the two set of analysis and it is possible to use, instead of two set of results only one, the average concentration and the average standard deviation computed from the results determined with the two spectrometers:

$$\bar{x} = \frac{\bar{x}_1 + \bar{x}_2}{2} \tag{8}$$

$$s = \sqrt{\frac{\sum_i (x_{i1} - \bar{x}_1)^2 + \sum_i (x_{i2} - \bar{x}_2)^2}{n_1 + n_2 - 2}} \tag{9}$$

where x_{i1}, x_{i2}, $\bar{x}_1$ and $\bar{x}_2$ represents the individual results of the parallel measurements (n_1, n_2) and the correspondent averages of those series, obtained with the two ICPs. Thus, the result of elemental analysis via ICP – OES technique will be represented by the general formula:

$$\bar{x} \pm s \tag{10}$$

3. Results and discussion

3.1 Analysis of the Certified Reference Material $Bi_2Sr_2Ca_1Cu_2O_8$ (x = 0,15 – 0,20)

The 2212 type ALDRICH superconductor, with ICP – OES certified elemental concentrations, was analysed with both ICPs (SPECTROFLAME and SPECTRO CIROS^{CCD}) in order to certify the technique. The results are presented as compared to the certified concentrations in Table 2.

Table 2.

Elemental concentrations (m/m) for the Certified Reference Material obtained via ICP–OES for n = 5 parallel measurements, as compared to the certified concentrations

	Bi	**Sr**	**Ca**	**Cu**
certified concentrations	**41**	**20**	**4.3**	**13**
SPECTROFLAME	41.8 ± 2.0	20.1 ± 0.5	4.2 ± 0.2	13.4 ± 0.4
SPECTRO CIROS^{CCD}	41.3 ± 1.6	19.8 ± 0.3	4.4 ± 0.2	13.1 ± 0.4
average concentration ± $s_{average}$	**41.6 ± 1.8**	**20.0 ± 0.4**	**4.3 ± 0.2**	**13.3 ± 0.4**

The stoichiometric ratios calculated using the standard procedure are presented in Table 3.

Table 3.

Stoichiometric coefficients and standard deviations calculated for results from Table 2.

certified	**$Bi_{1.87 \pm 0.12}$ $Sr_{2.17 \pm 0.14}$ $Ca_{1.02 \pm 0.07}$ $Cu_{1.95 \pm 0.13}$**
SPECTROFLAME	$Bi_{1.89 \pm 0.11}$ $Sr_{1.99 \pm 0.12}$ $Ca_{0.99 \pm 0.06}$ $Cu_{1.99 \pm 0.11}$
SPECTRO CIROS^{CCD}	$Bi_{1.87 \pm 0.11}$ $Sr_{2.13 \pm 0.13}$ $Ca_{1.04 \pm 0.06}$ $Cu_{1.95 \pm 0.12}$
average ± $s_{average}$	**$Bi_{1.88 \pm 0.12}$ $Sr_{2.13 \pm 0.14}$ $Ca_{1.01 \pm 0.06}$ $Cu_{1.96 \pm 0.12}$**

The statistical validation proved that there are no systematic errors and significant differences between our determinations and the certified values. Also, there are no signifficant differences between the calculated average stoichiometric coefficients and the theoretical, as this is proved by data from Table 4.

Table 4.

Statistical validation of the experimental formula by means of t – test

Theoretical formula	**$Bi_2Sr_2Ca_1Cu_2O_{8+x}$ (x = 0.15 – 0.20)**			
Experimental formula	**$Bi_{1.88 \pm 0.12}$ $Sr_{2.13 \pm 0.14}$ $Ca_{1.01 \pm 0.06}$ $Cu_{1.96 \pm 0.12}$**			
$t_{calculated}$	2.04	1.81	0.32	0.69
$t_{tabulated}$	2.78 (P = 95 % and ν = n – 1 = 5)			

3.2 Analysis of the $Y_{0,95}Bi_{0,05}Ba_2Cu_3O_x$ sample

The experimental measurements were carried out via atomic emission technique, with both SPECTROFLAME and SPECTRO CIROS^{CCD} spectrometers equipped with ICP.

The results of 5 parallel measurements as compared to the theoretical concentration calculated according to the stoichiometry of the compound is presented in Table 5. The average concentration was calculated from the two averages obtained with the two ICPs.

Using t – test (Eq.6) it was checked if there is any significant difference between the two averages. In this case t_{tab}= 2.31 for a probability of P = 95 % and $\nu = 5 + 5 - 2 = 8$ degrees of freedom. As it is shown by Table 6 t_{calc} is smaller than t_{tab}, therefor there are no significant errors between the two averages. The standard deviation were tested by means of F – test (Eq.5) and it was found that there are no systematic errors between the standard deviations ($F_{calc} < F_{5,5} = 5.050$ for P = 95 %, $\nu_1 = 5$ and $\nu_2 = 5$). Thus it was possible to calculate the average standard deviation using s_1 and s_2.

Both ICPs were tested according to t – test (Eq.1) in order to decide if there are significant errors between the results obtained with the plasma sources, on one hand, and the theoretical concentration calculated from stoichiometry, on the other hand. As it is shown in Table 7 $t_{calc} < t_{tab}$ for P = 95 % and $\nu = 5 - 1 = 4$, thus there are no significant errors between the theoretical concentrations and the results of concentration determinations via inductively coupled plasma source atomic emission spectroscopy.

Table 5.

Elemental concentrations (m/m) in sample $Y_{0,95}Bi_{0,05}Ba_2Cu_3O_x$ obtained via ICP – OES for n = 5 parallel measurements, as compared to theoretical concentration calculated from theoretical stoichiometry of the compound

	Y	**Bi**	**Ba**	**Cu**
theoretical concentration	**12.56**	**1.54**	**40.86**	**28.34**
SPECTROFLAME	12.71 ± 0.50	1.58 ± 0.30	40.76 ± 1.10	28.50 ± 0.60
SPECTRO CIROS^{CCD}	12.48 ± 0.30	1.55 ± 0.20	40.56 ± 1.25	28.30 ± 0.40
average concentration ± $s_{average}$	**12.60 ± 0.40**	**1.57 ± 0.25**	**40.66 ± 1.18**	**28.40 ± 0.51**

Table 6.

Values of the t coefficient as they resulted by comparing the results obtained with the two plasmas

	Y	**Bi**	**Ba**	**Cu**	**$t_{tabulated}$**
$t_{calculated}$ *	0.88	0.19	0.27	0.62	2.31 **

Table 7.

Values of the t coefficient as they resulted by comparing the results obtained with the two plasmas with the theoretical concentration

	Y	**Bi**	**Ba**	**Cu**	**$t_{tabulated}$**
SPECTROFLAME	0.67	0.3	0.61	0.60	2.78 **
SPECTRO CIROS^{CCD}	0.60	0.11	0.54	0.22	

The stoichiometric coefficients were calculated according to the standard procedure. Thus, for each plasma four values were obtained. They were statistically tested using Dixon's Q – test (Eq.2). The result of this test proved that there are no significant differences, therefor the averages of the stoichiometric coefficients and of the standard deviations were calculated using those four values. Similarly, using t– and F– tests it was found that there are no systematic errors between the two plasma sources. The average coffiecients and standard deviations were also calculated (Table 8). As compared to the theoretical stoichiometry (Y: Bi: Ba: Cu = 0.95: 0.05: 2: 3) there were no significant errors.

Table 8.

Stoichiometric coefficients and standard deviations calculated using the results from Table 5 and the standard methodology

theoretical	**$Y_{0.95}Bi_{0.05}Ba_{2}Cu_{3}$**
SPECTROFLAME	$Y_{0.95 \pm 0.01}Bi_{0.050 \pm 0.001}Ba_{1.98 \pm 0.02}Cu_{2.99 \pm 0.02}$
SPECTRO CIROS^{CCD}	$Y_{0.95 \pm 0.01}Bi_{0.050 \pm 0.001}Ba_{1.99 \pm 0.01}Cu_{3.00 \pm 0.01}$
average ± $s_{average}$	**$Y_{0.95 \pm 0.01}Bi_{0.050 \pm 0.001}Ba_{1.99 \pm 0.02}Cu_{2.99 \pm 0.02}$**

3.3 Analysis of the $Bi_2Sr_2Ca_{0,9}Gd_{0,1}Cu_2O_x$ sample

The analysis were performed in a similar way they were done for the $Y_{0,95}Bi_{0,05}Ba_2Cu_3O_x$ sample. The results are presented in Tables 9 – 12.

Table 9.

Elemental concentrations (m/m) in sample $Bi_2Sr_2Ca_{0,9}Gd_{0,1}Cu_2O_x$ obtained vis ICP – OES for n = 5 parallel measurements, as compared to theoretical concentration calculated from theoretical stoichiometry of the compound

	Bi	**Sr**	**Ca**	**Gd**	**Cu**
theoretical concentration	**46.44**	**19.47**	**4.01**	**1.75**	**14.12**
SPECTROFLAME	46.24± 0.38	19.33± 0.50	3.95 ± 0.25	1.77 ± 0.10	14.26 ± 0.23
SPECTRO CIROS^{CCD}	46.50± 0.25	19.42± 0.32	4.02 ± 0.18	1.74 ± 0.08	14.18 ± 0.15
average concentration±$s_{average}$	**46.37± 0.32**	**19.38± 0.42**	**3.99 ± 0.22**	**1.76 ± 0.09**	**14.22 ± 0.19**

Table 10.

Values of the t coefficient as they resulted by comparing the results obtained with the two plasmas

	Bi	**Sr**	**Ca**	**Gd**	**Cu**	$t_{tabulated}$
$t_{calculated}$ *	1.28	0.34	0.51	0.52	0.65	2.31 **

Table 11.

Values of the t coefficient as they resulted by comparing the results obtained with the two plasmas with the theoretical concentration

	Bi	**Sr**	**Ca**	**Gd**	**Cu**	$t_{tabulated}$
SPECTROFLAME	1.18	0.63	0.54	0.45	1.36	
SPECTRO CIROS^{CCD}	0.54	0.35	0.12	0.28	0.89	2.78 **

Table 12.

Stoichiometric coefficients and standard deviations calculated using the results from Table 9 and the standard methodology

theoretical	$\mathbf{Bi_2\ Sr_2\ Ca_{0.9}\ Gd_{0.1}\ Cu_2}$
SPECTROFLAME	$Bi_{1.99 \pm 0.02}\ Sr_{1.99 \pm 0.02}\ Ca_{0.89 \pm 0.01}\ Gd_{0.100 \pm 0.001}\ Cu_{2.02 \pm 0.02}$
SPECTRO CIROS^{CCD}	$Bi_{2.00 \pm 0.01}\ Sr_{1.99 \pm 0.01}\ Ca_{0.90 \pm 0.01}\ Gd_{0.099 \pm 0.001}\ Cu_{2.01 \pm 0.01}$
average ± $s_{average}$	$\mathbf{Bi_{1.99 \pm 0.02}\ Sr_{1.99 \pm 0.02}\ Ca_{0.90 \pm 0.01}\ Gd_{0.100 \pm 0.001}\ Cu_{2.02 \pm 0.02}}$

As compared to the theoretical stoichiometry (Bi: Sr: Ca: Gd: Cu = 2: 2: 0.9: 0.1: 2) there are no significant errors.

4. Conclusions

In this paper the elemental composition of superconducting oxides $Y_{0.95}Bi_{0.05}Ba_2Cu_3O_x$ and $Bi_2Sr_2Ca_{0.9}Gd_{0.1}Cu_2O_x$ was studied using inductively coupled plasma atomic emission spectroscopy (ICP-OES). In order to ensure the quality control of both superconducting materials preparation recepies and preparation technologies, the elemental content (concentrations and stoichiometric coefficients) of $Y_{0.95}Bi_{0.05}Ba_2Cu_3O_x$ and $Bi_2Sr_2Ca_{0.9}Gd_{0.1}Cu_2O_x$ superconducting samples was investigated via inductively coupled plasma source atomic emission spectroscopy technique. The technique was certified by analysing a 2212 type superconductor. The optimal operating conditions, line selections and detection limits were discribed for two ICP spectrometers, a secvential (SPECTROFLAME) and simultaneous one (SPECTRO CIROS ^{CCD}). The results of our investigations are in good agreement with the other, magnetical or structural type of investigations. This type of investigation, due to its nature, could also be very useful is establishing if the annealing of superconducting materials affects in same way the stoichiometry of the samples.

REFERENCES

[1] L. Paama, P. Peramaki and L.H.J. Lajunen: Analytica Chimica Acta **330** (1996) p. 259

[2] R. Kucharkowski, C. Vogt, D. Marquardt: Fresenius J. Anal. Chem **366** (2000) p.146

[3] D. Geilenberg, M. Gerards, J.A.C. Broekaert: Mikrochim. Acta **133** (2000) p.319

[4] M.J. Kulkarni, A.A. Argekar, S.K. Thulasidas, A.G. Page and M.D. Sastry: Fresenius J. Anal. Chem **342** (1992) p.367

[5] M.M. Pop: MSc. Thesis, Babes-Bolyai University, Faculty of Physics, Cluj, 1996

[6] J.C. Miller and J.N. Miller: „Statistics for Analytical Chemistry" Ellis Hrowood Ltd. 1988

STUDIA UNIVERSITATIS BABEŞ-BOLYAI, PHYSICA, XLVIII, 1, 2003

SPIN GLASS IN Gd RICH $U_{1-x}Gd_xAl_4$ SYSTEM

ILEANA LUPSA[1]

ABSTRACT. The magnetic and structural study of $U_{1-x}Gd_xAl_4$ (x=0. 8 and 0. 6) system was performed. The magnetic properties investigated in the 4-600 K temperature range and fields up to 90 kOe showed the magnetic order presence. The magnetic behaviour evidenced a transition from the ferromagnetic one (x=0) to the spin glass (x≤0. 8). The change in the magnetic properties is correlated to the substitutional disorder which manifests in the Gd clusters having easy axis randomly aligned superposed on the spin fluctuations due to uranium atoms.

Keywords: Uranium compound; Rare earth compound; Magnetic properties; Spin fluctuations

Introduction

The $GdAl_4$ has the UAl_4 orthorhombic type symmetry. The magnetic behaviour is ferromagnetic with a transition temperature T_c=163 K, a spontaneous magnetization of 6. 9 μ_B/f. u. and an effective magnetic moment in the paramagnetic region of 7. 94 μ_B [1, 2]. The UAl_4 compound crystallizes in the orthorhombic UAl_4 type structure having lattice parameters very close to that of $GdAl_4$. The compound is reported having a maximum in the temperature dependence of the susceptibility at 200 K; over 400 K is a Curie-Weiss paramagnet with a negative paramagnetic Curie temperature (-850 K) and an effective magnetic moment of 3.. 9 μ_B [3]. The compound presents the spin fluctuations behaviour characteristics.

The present paper intends to establish the influence of a magnetic rare-earth substitution studying the $U_{1-x}Gd_xAl_4$ gadolinium rich system. We report the magnetic behaviour results on the polycrystalline $U_{1-x}Gd_xAl_4$ system for x=0. 8 and 0. 6, our study evidencing a rapid transition from the ferromagnetic order to the spin glass one.

Experimental details

The polycrystalline samples $U_{1-x}Gd_xAl_4$ were prepared by stoichiometric amounts of the elementary metals (3 N purity for U and better for the others) in an argon arc furnace in a protective purified atmosphere; several times melting assured a good homogeneity.

The standard X-ray diffraction method for phase purity, the crystal type structure and the lattice parameters determination was used. The analyses indicated the presence of the orthorhombic phases with a slow modification in the lattice constants as Gd replaces for U sites.

[1] *Technical University,3400 Cluj-Napoca,Romania; Department of Physics, Technical University Str. C. Daicoviciu,nr.15,3400 Cluj-Napoca, Romania Email: ileana.lupsa@phys.utcluj.ro*

The magnetic measurements were performed in the 4-600 K temperature range and fields up to 90 kOe. The systems having x≥0. 6 are magnetically ordered.

In the high temperature range the systems present paramagnetic behaviour of the Curie-Weiss type. The susceptibility accurate values χ were determined using the Honda-Owen rule: $\chi_m=\chi+cM_s'H^{-1}$. Plotting the experimental susceptibility χ_m versus the reciprocal magnetic field, the correct susceptibility was obtained for $H^{-1} \rightarrow 0$. The influence of the possible magnetic impurity having concentration c and the saturation magnetization M_s' was in this way eliminated.

Results

The systems having x. >0. 6 are magnetically ordered. The transition temperatures T_c respect an almost linear increasing as Gd content becomes higher. The field dependence of the M values for x=0. 8 is represented in Fig. 1.

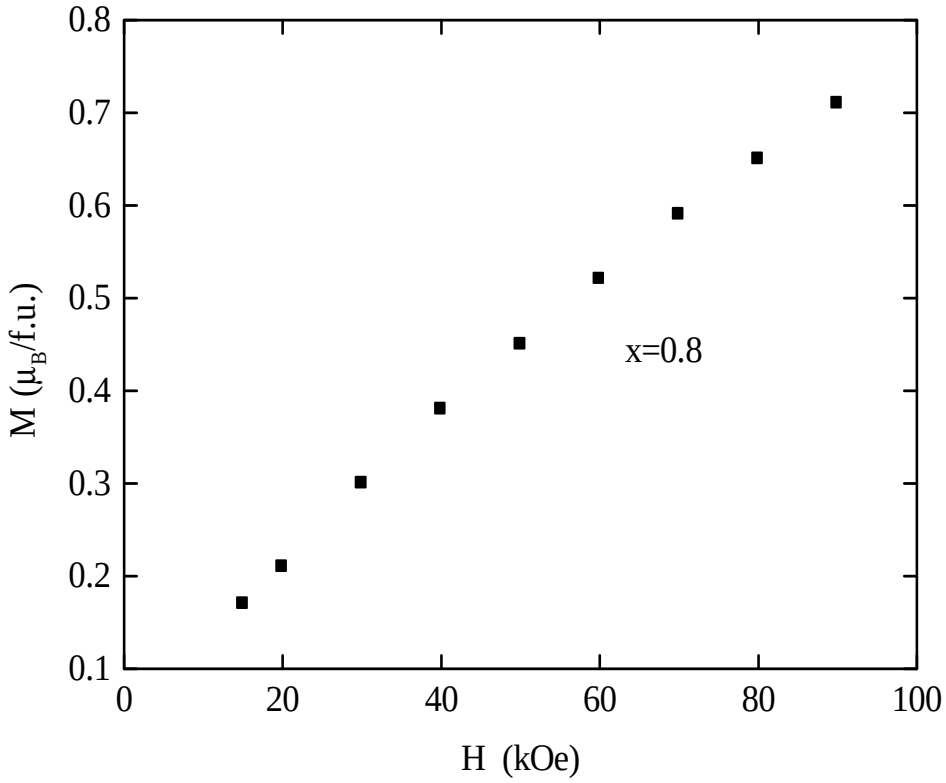

Fig. 1. The field dependence of the magnetization values at 4. 2 K

The saturation of magnetization is not completely reached even in 90 kOe magnetic field. The d. c. thermal susceptibility variation in the low magnetic field (300 Oe and 600 Oe) evidences the sharp maxima in χ values suggesting the presence of the spin glass order state (Fig. 2). A such behaviour is reported by Coles [4] about the magnetic properties of the $U_{1-x}Gd_xAl_2$ system also in the high Gd composition. As seen in Fig. 2 the cusp at the freezing temperature in the susceptibility in the low field is present.

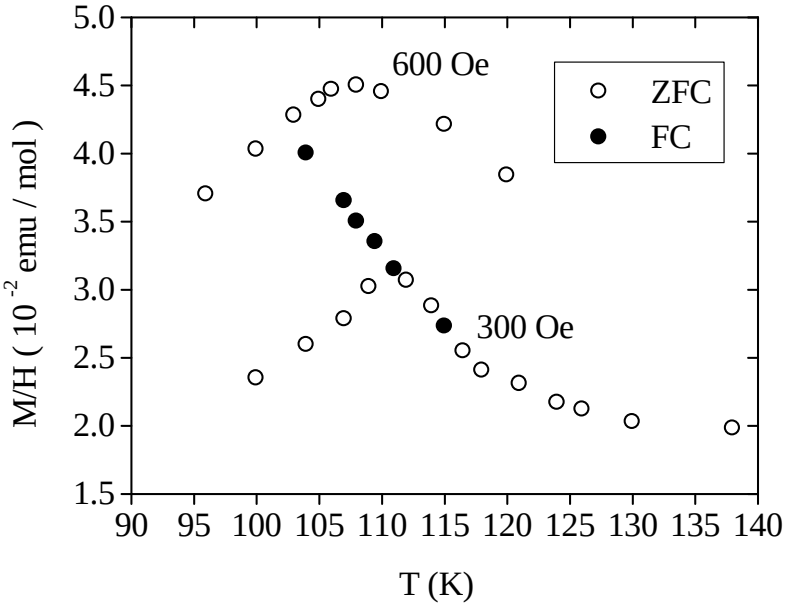

Fig. 2. The thermal dependence of the dc susceptibility for $U_{0.2}Gd_{0.8}Al_4$. ZFC measurements are reported for 300 and 600 Oe and ZC data are presented for 300 Oe.

The temperature dependence of the zero field cooled (ZFC) reduced magnetization indicate that the cusp is located at different temperature presenting a sensitivity to the external magnetic field values. The both freezing temperatures are lower than the transition T_c temperature. The sharp cusp observed in 300 Oe is at 115 K located. The freezing temperature is shifted to lower temperatures with increasing magnetic field. The Fig. 2 also displays the field-cooled (FC) reduced magnetization for 300 Oe. The magnetization depends of the cooling process, FC and ZFC curves are different and the irreversibility starts from the temperature near the cusp temperature. In the ZFC it is generated a remanence magnetization which relaxes over a long time; a metastable and irreversible state is generated by the magnetic field. The FC magnetization presents reversibility with temperature for a fixed field. These features are characteristics of randomly quenched spin ordering as spin glass state is.

The paramagnetic behaviour follows a Curie-Weiss type law: $\chi = C/(T-\theta)$. The reciprocal susceptibility dependence vs temperature is plotted in Fig. 3. The paramagnetic Curie temperatures θ are negative and decrease as Gd substitutes for U sites. The molar Curie constants C are increasing from 7. 9 emu K/mol the value reported for $GdAl_4$ to 5. 48 emu K/mol corresponding to x=0. 6. In the assumption that the magnetic susceptibility is due to the superposition of two effects, due to uranium atoms and the other one caused by the gadolinium we separated the gadolinium influence. The U atoms contribution in C is obtained and the effective magnetic moments per U atoms were calculated. These values are composition independent, the μ_{eff} /U atom has the same value of 3. 9 μ_B obtained in UAl_4, for every sample supporting that the spin fluctuations associated to uranium atoms are not suppressed by Gd internal field.

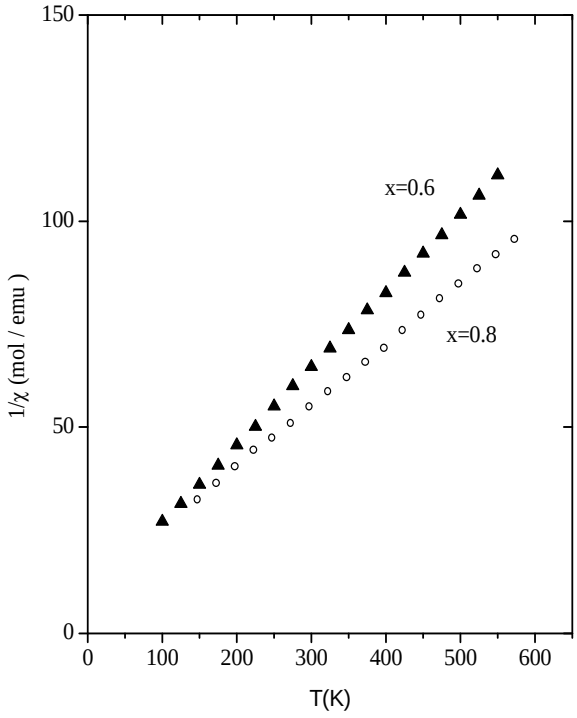

Fig. 3. The temperature variation of the reciprocal susceptibility of $U_xGd_{1-x}Al_4$ system.

Discussion

The magnetization isotherms are characteristic for a mictomagnetic or spin glass behaviour. The magnetization in field of 90 kOe at 4. 2 K decreases from 7 μ_B/f. u (x=0) to 2. 5 μ_B/f. u (x=0. 8) and 2. 25 μ_B/f. u for x=0. 6. The high decrease can be explained only if the magnetic moments of gadolinium are not parallely oriented. To analyze this behaviour dc measurements were made. The data obtained for a sample with x=0. 8 show a typical spin glass behaviour. The paramagnetic region results indicate a superposition of Gd^{3+} and U^{3+} contributions.

The gadolinium in the present system shows a well localized magnetic behaviour, as evidenced in $GdAl_4$. The saturation moment at 4. 2 K is close to 7 μ_B, while in the paramagnetic range the effective moment is 7. 94 μ_B, typical for Gd^{3+} ion. Uranium is paramagnetic and shows the same effective magnetic moment as in UAl_4. The magnetic behaviour of UAl_4 can be analyzed in model that takes into account the electron correlation effects in f band as the spin fluctuations model is These characteristics are specific to the spin fluctuations system and UAl_4 was discussed in the selfconsistent renormalization theory of spin fluctuations (SCR) [5, 3]. The dynamical susceptibility for low wave vectors q values is temperature dependent and leads to an average amplitude of the spin fluctuations increasing with increasing T. At the characteristic temperature T* it becomes constant and the systems over T* present a Curie-Weiss type paramagnetism like those compounds which have a local magnetic moment. For the systems with high exchange enhancement factors the amplitude of the spin fluctuations is saturated and the effective magnetic moment is close to that of the free ion U^{3+} (3. 62 μ_B). In $U_{1-x}Gd_xAl_4$ for $x \geq 0.6$ it seem to be present such saturated thermal induced spin fluctuations, the effective magnetic moment per U atom maintains the same value.

When replacing gradually gadolinium by uranium, the Curie temperature decreases gradually from 152 K (x=1) to -40 K (x=0. 6). In addition the type of magnetic ordering changes. In the high gadolinium concentration range (x=0. 8) a spin glass type behaviour is shown. As it is reported for $GdAl_2$ a spin glass type behaviour may be induced by milling [6]. The mechanical milling causes a disorder responsible for changing the number of the nearest Gd-Gd neighbours. In our system a substitutional type of disorder is generated. This leads to the change in the originally parallel direction of the Gd moment as ferromagnet to a randomly distributed alignment. In these conditions ferromagnetic and antiferromagnetic mixed interactions may be present. This fact is evidenced in the low field magnetization at 4. 2 K. These values are lower than the expected for Gd^{3+} and the 90 kOe field is not able to align in the same direction all the randomly distributed Gd moments. We suppose that there are clusters of gadolinium atoms, the magnetization of cluster having different easy axis of magnetization. The magnetic moments of the clusters are mainly antiferromagnetic oriented as evidenced by the low value of the magnetization. The negative paramagnetic Curie temperatures θ are in agreement with the predominance of the negative contributions to the exchange interactions.

REFERENCES

1. R. H. J. Buschow, Rep. Prog. Phys. 40 (1977) 1179

2. H. Oestereicher, J. Less-Common Metals 55 (1977) 135

3. I. Lupsa, P. Lucaci, E. Burzo, J Alloys Compound 298 (2000) 40

4. B. R. Coles, J. Z. Ping and M. H. Bennett, Philosophical Magazine B 50 (1984) 1

5. T. Moriya, J. Magn. Magn. Mater., 14 (1979) 1

6. G. F. Zhou and H. Bakker, Phys. Rev. B52(1995) 9437

STUDIA UNIVERSITATIS BABEŞ-BOLYAI, PHYSICA, XLVIII, 1, 2003

FOURIER ANALYSIS OF THE OSCILLATIONS OF A CCP GENERATOR

S. D. ANGHEL, A. SIMON, L. HOBAJ[1]

ABSTRACT. Fourier transform method is used in order to analyze the influence of the capacitively coupled plasma maintained in air at atmospheric pressure on the signal coming from the RF generator used to ignite and maintain the discharge. The plasma is ignited in the resonant circuit of the RF oscillator. The presence of the plasma in that circuit modifies the spectral composition of the RF signal in function of the absorbed power into the plasma.

Introduction

The radiofrequency (RF) capacitively coupled plasma (CCP) generated in various gases (air, argon, helium) at atmospheric pressure has been used for about twenty years in two main directions: spectroscopy and material processing.

One of the first scientists who studied systematically CCP at atmospheric pressure was R. Grigorovici [1,2]. He studied electric properties and the emission spectra of CCP generated in various gases.

An electric model can be associated with plasma generated in a variable electromagnetic field. This model is based on the electrical impedance of the plasma which has a real component (the resistance of the plasma) and an imaginary component (the reactance of the plasma). Because the plasma studied in the present work is the intrinsic part of the oscillating circuit of the RF generator, is evident that the waveform of the generated oscillations must be influenced by the electrical characteristics of CCP.

The aim of the work is to initiate a study to establish how CCP affects the waveform of the generated oscillations using the Fourier transform method (FTM).

Experimental set-up

The diagram of the plasma generator which was used in this study was described in previous works [3, 4]. The plasma is sustained in air at atmospheric pressure at a frequency of 17.95 MHz. The experimental set-up, which was used for analysis of spectral composition by FTM, is shown in Fig.1.

[1] *"Babes-Bolyai" University, Faculty of Physics, 3400 Cluj-Napoca, Romania*

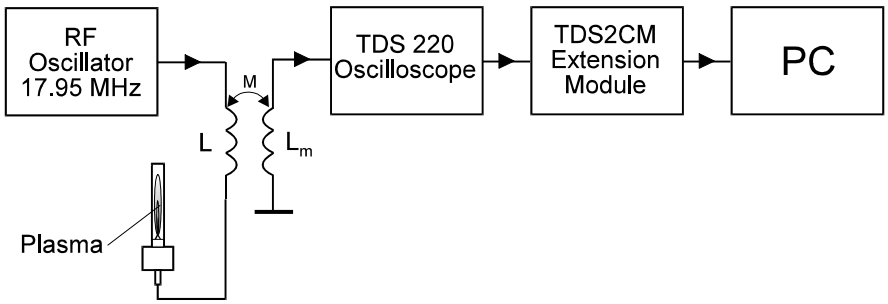

Fig. 1. Experimental set-up.

The digital real-time oscilloscope (TDS 220 – Tektronics) has incorporated an extension module (TDS2CM) for acquiring and transferring of binary data to the PC. The waveform of the generated oscillations is registered via coil L_m, inductively coupled with coil L, from the resonant circuit of the RF oscillator. The RF signal is visualized on the screen of the oscilloscope and on the PC monitor via the RS-232 interface. The acquisition rate of the signal is 500 samples per second. So, the condition imposed by the sampling theorem is satisfied from DC (0 Hz) to the Nyquist frequency (250 MHz). In order to reduce random or uncorrelated noise in the signal displaying, the average acquisition mode was used. The number of acquisitions to average for the waveform was 128. The fast Fourier analysis was performed with the software WSTRO WaveStar (Tektronix).

Results and discussions

The measurements and the Fourier analysis of the generated signal was performed in the absence of the plasma and in the presence of it, under two experimental conditions: anodic tension, E_a (the continuous tension which powered the oscillator) equal with 900V and 1000V, respectively. These two values correspond to two powers absorbed by the plasma: 30,6 W and 47 W.

In order that the signal not be affected by the noise, ten spectra aquisited under the same conditions were added and mediated using a software written in Turbo Pascal 7.0.

The plots of the Fourier spectra of the signal generated under the above two conditions, in the absence of the plasma and in the presence of it are presented in Fig.2 and Fig.3. We mention that the amplitude of –36 dB means the absence of a spectral line from the Fourier spectrum or the fact that a spectral line is up-to noise level.

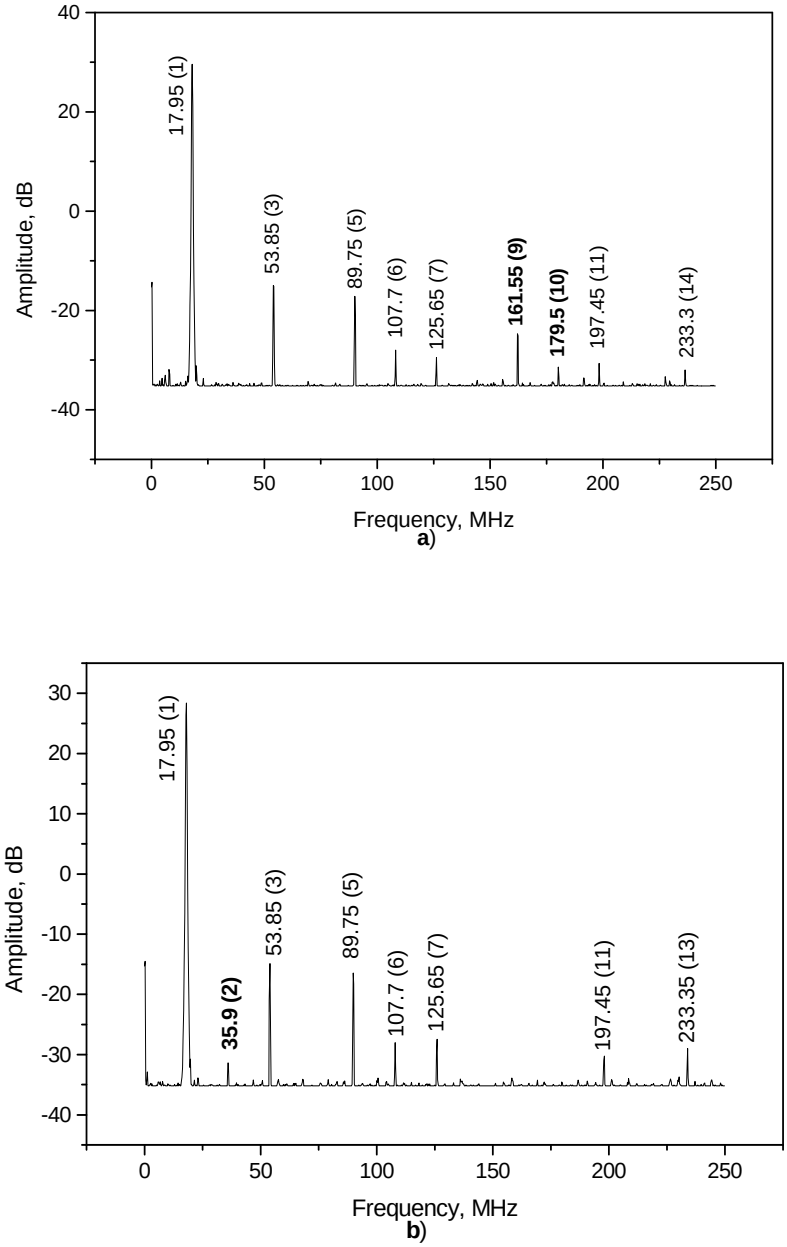

Fig. 2. Fourier spectrum of the signal generated at E_a = 900V: a) in the absence of the plasma and b) in the presence of the plasma (30.6 W).

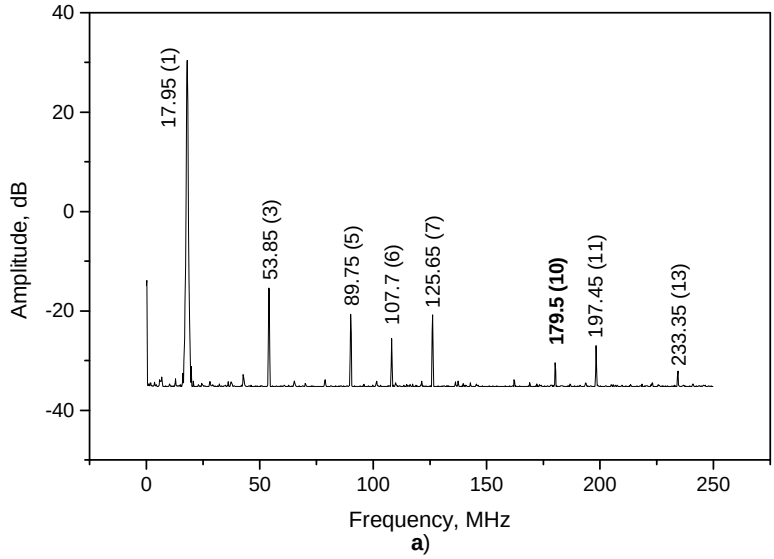

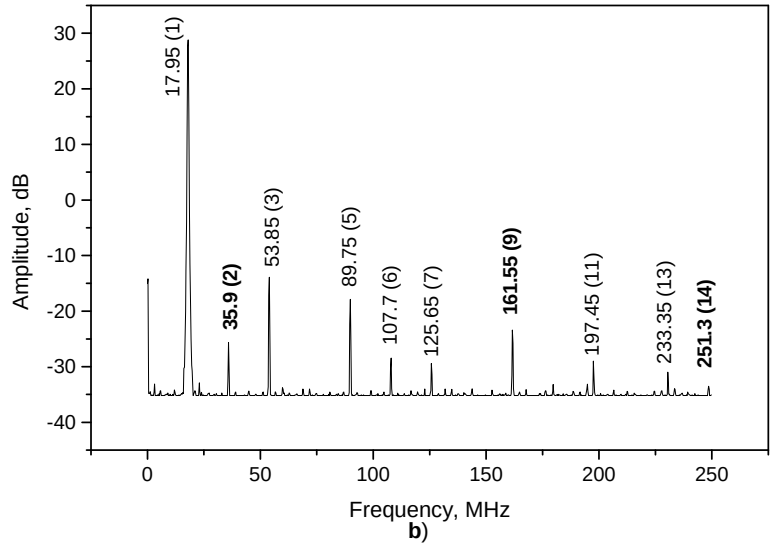

Fig. 3. Fourier spectrum of the signal generated at E_a = 1000V:
a) in the absence of the plasma and b) in the presence of the plasma (47 W).

Comparing the Fourier spectra of the signals in the absence and in the presence of the plasma, the following conclusions can be drawn:

i. There are two ways in which the plasma influences the spectral composition of the generated signal: a) the attenuation of the fundamental frequency and of its harmonics. This is a result of the amplitude decreasing of the RF oscillations in the presence of the plasma as a consequence of the absorbed power from the electromagnetic field. b) the appearance or disappearance of some harmonics of the fundamental frequency. Thus, the presence of the 30.6 W plasma determines the appearance of the 2^{nd} harmonic (35.9 MHz) of the fundamental frequency and the disappearance of the 9^{th} and 10^{th} harmonics (161.55 MHz and 179.5 MHz respectively). In the presence of the 40 W plasma, the Fourier spectrum is lacked of the 10^{th} harmonic (179.5 MHz) but it has three new harmonics: the 2^{nd} (35,9 MHz), the 9^{th} (161.55 MHz) and the 14^{th} (251.3 MHz). A possible explanation of the appearance and disappearance of some harmonics in the presence of the plasma can be the changing of the functioning static point on the transfer characteristic of the oscillating tube. This characteristic has a nonlinear aspect.

ii. The higher plasma power the more changes of the Fourier spectrum.

iii. The fact that in the presence of the plasma do not appear signals having different frequencies on the harmonics of the fundamental frequencies, drives us to the conclusion that neither the capacitance nor the inductance of the plasma have values capable of modifying the capacitance or the inductance of the resonant circuit of the RF oscillator.

This research was supported by Research Grant 34/1260, CNCSIS/2002.

REFERENCES

1. [1] G.Cristescu, and R.Grigorovici, “Study of high frequency torch. Measurements of voltage, current and power,” *An. Acad. RPR*, **3**, 63-78 (1949).
2. [2] G.Cristescu, and R.Grigorovici, “Study of high frequency torch. Spectroscopic studies,” *Com. Acad. RPR*, **5**, 515-522 (1955).
3. [3] E.Tataru, S.D.Anghel, and I.I.Popescu, “A stabilized low power r.f. torch discharge for analytical spectrometry,” *Rev. Roum. Phys*., **36**, 29-44 (1991).
4. [4] S.D.Anghel, “Generation of a Low-Power Capacitively Coupled Plasma at Atmospheric Pressure”, IEEE Trans. Plasma Sci. **30**, (2002 – in press).

STUDIA UNIVERSITATIS BABEŞ-BOLYAI, PHYSICA, XLVIII, 1, 2003

PHOTOPHYSICAL PARAMETERS FOR EL-4 CELLS INACTIVATION IN PHOTODYNAMIC THERAPY OF CANCER

RODICA-MARIANA ION*[1], LUCIA SAVI, G.SAVI[2], V. I. R. NICULESCU[3]

***ABSTRACT*.** Photodynamic therapy (PDT) of tumor is an indirect method for cancer treatment by the combined action of oxygen, light and different photosensitizers-drugs, porphyrins being the most used between them.

Several parameters for porphyrin dyes, used as sensitizers for PDT aluminum porphyrin tetrasulphonate with different axial ligands C2, C4, C8 and C12, are evaluated in this paper, as follows:

- absorption, fluorescence-excitation and fluorescence-emission spectra of the cell-bound dyes;
- relative quantum yields for photoinactivation of EL-4 cells (prelevated from singenic mice C57 Bl/6) after 18 hours incubation with the dyes;
- relative quantum yields of photodegradation of the singlet oxygen trap-1,3-diphenylisobenzofuran (DPBF) in cells after 18 h incubation with the dyes;
- data processing with Fast Fourier Transform for singlet oxygen quantum yield;
- partition coefficients in 2-octanol-water system.

Keywords: porphyrins, photodynamic therapy, EL-4 cells.

1. INTRODUCTION

Photodynamic therapy (PDT) of cancer has been known for over twenty years and is based on the dye-sensitized photooxidation of biological targets in the tumoral tissue [1].

In spite of intensive research, the information on the mechanisms controlling the response of malignant lesions to this phototherapeutic modality are still largely incomplete. In fact, the action of PDT can involve various subtissular targets, including the neoplastic cells, the blood cells and the non-vascular stroma [2-7], the PDT-induced tumor damage occuring via apoptotic pathways. Reactive oxygen species cause both cell death and damage to blood vessels thus contributing to tumor regression.

[1] *Institute for Chemical Research, Chemical Analysis Dept., Splaiul Independentei 202, Bucharest-77208, Romania; E-mail: irma@pcnet.ro*

* The correspondence author

[2] *Institute for Pathology and Biomedical Sciences "V. Babes", Bio-base Dept., Splaiul Independentei 201, Bucharest-76201, Romania*

[3] *National Institute for Lasers, Plasma and Radiation Physics, Magurele-Bucharest; P.O. Box MG-36; Romania; E-mail: nicval@ifin.nipne.ro*

PDT is widely influenced by the physico-chemical structure of the drug, in particular the degree of hydrophobicity [8] and also, by the photostability of all these sensitizers [9-12]. Therefore, it appears important to optimize the development of second generation photosensitizers with improved selectivity of tumor.

The most extensively studied in relation to photodynamic therapy are porphyrins [13,14]. Due to their high number of double bonds, porphyrins have a strong absorption peak at about 400 nm (the Soret band) and a number of minor peaks at longer wavelengths up to about 630 nm. From photochemical point of view, porphyrins are good photosensitizers in spite of their low photostability. Porphyrins were shown to be non toxic when given in high doses for long periods of rabbits, mice, pigs, cats and dogs [15].

Porphyrins can be chelated with a variety of metals, the diamagnetic ones enhancing the phototoxicity. Paramagnetic metals are shortening the lifetime of the triplet state and as result can make the dyes photoinactive [14].

The photosensitizing activity is quenched by the presence of transition metal ions (as central ions) with a d-electron configuration [16].

The presence of axial ligands to the centrally coordinated metal ion is often advantageous, since it generates some degree of steric hindrance to intermolecular aggregation, without impairing the photophysical properties of the dye.

Several photophysical parameters for aluminum porphyrins tetrasulphonated are evaluated in this paper, using in vitro experiments on EL-4 cells.

2. EXPERIMENTAL PART

2.1. Chemicals

For this paper, were synthesized the following compounds:

TSPP (5,10,15,20-tetra-sulphonato-phenyl-porphyrin);

C2AlTSPP (ethyl-aluminum 5,10,15,20-tetra-sulphonato-phenyl-porphyrin);

iC4AlTSPP(isobuthyl-aluminum-5,10,15,20-tetra-sulphon1ato-phenyl-porphyrin);

C8TSPP (octyl-aluminum- 5,10,15,20-tetra-sulphonato-phenyl-porphyrin);

C12AlTSPP (dodecyl-aluminum-5,10,15,20-tetra-sulphonato-phenyl-porphyrin).

Structural formulas of the dyes tested in this paper are shown in Figure 1.

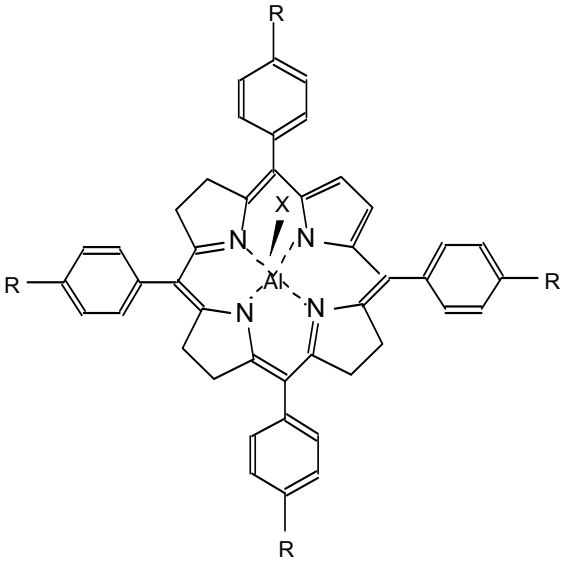

Fig. 1. The structure of AlX-TRPP (R = SO_3; X=C_2, C_4, C_8, C_{12}). Their preparation have been reported elsewhere [17].

All these photosensitizers have been solubilized in water pH 7.4. Small aliquots from the stock solutions were added directly to the culture medium.

1,3-Diphenyl-isobenzofuran (DPBF) was synthesized in the lab from a literature receipt [18].

EL-4 cells were prelevated from leukemia mice, after a specific procedure as follows: the lymphoma leukemia EL-4 cells have been obtained from syngenically mice C57 Bl/6 in V.Babes Institute. They are kept in some plastic boxes with free access at food and water. The ascetic form of this tumoral line is kept by means of some i.p.weekly passages [19]. After 5-6 days post-inoculation of 10^5 tumoral cell, the ascetic animals have been sacrificed, collecting in sterile conditions the ascetic liquid by washing of the peritoneal cavity with 3-4 ml of physiologic serum. The suspension of tumoral cells have been washed three times by centrifugation with physiologic serum, after that being measured the viability with trypan, the value being 80-90%. After deposition, the cells have been resuspended in physiological serum and counted, repeating the viability test with trypan. The tumoral cells ($1x10^4$) have been cultivated in medium (RPMI-1640) supplemented with antibiotics and 10% cow phoetal serum [20] on 35 mm plates, $1x10^4$ cells. After 48-72 hours from the cultivation, the adherent cells have been collected with 0.125 % tripsine and 0.01% EDTA in physiological serum. All the cells are measured between 10^5-10^6 and 10^7 per plate.

The prepared cells have been incubated with tested compounds. After an incubation period of 24 h at 37^o C the cells were exposed to light in the presence of the drugs. The light source was a 375 W mercury lamp (Hg medium pressure). To

calculate intracellular drug concentrations it was used the absorption spectra of suspensions of known cell densities (and assumed a cellular volume of 2.3 x 10^{-3} ml).

2.2. Absorption and fluorescence measurements

Absorption spectra were recorded by means of a SPECORD M400 Carl Zeiss Jena spectrophotometer equipped with double beam and microprocessor. Quartz cuvettes with 1 cm optical path lengths and containing 2 ml of cell suspension each were used.

Fluorescence measurements were carried out in parallel with the absorption measurements using an Aminco-Bowmann spectrofluorimeter. A 1x1 cm cuvette containing 2 ml cell suspension was used. When recording the excitation spectra of porphyrins, a 580 nm cut-off filter was used to reduce the amount of scattered light, especially in the excitation region 230-350 nm.

2.3. Photodegradation of DPBF

The rate of DPBF photodegradation in cells was measured as follows: 5 μl DPBF was added to the cell suspension and let in contact 1 h. 2 ml of the cell suspension was placed in a 1x1 mm quartz cuvette and exposed to polychromatic light from a 275 nm medium pressure Hg lamp. DPBF was slowly photodegraded by 400-420 nm light. The amount of DPBF was monitored by absorption spectra and a subsequently deconvolution processing (Fast Fourrier Transform-FFT).

2.4. Fast Fourrier Transform (FFT) Processing of collected data

The procedure FFT are for computing in place the fast Fourrier transform FFT(x,y,z). The Fourrrier transform which is the classical machinery for investigating a broad range of applied problems. Usually Fast Fourrier Method is the first tool that an experimentalist uses in trying to get some informations from data. Numerical FFT are applied to a list of data of length N when N is equal to a power of two [21,22]. The first argument m should be a non-negative integer and the second and third arguments x and y should be array transform an output. The array y contains the imaginary part of the complex sequence on input and contains the imaginary part of the Fast Fourrier Transform on output.

2.5. Octanol/water partition coefficients

The partition coefficient between 1-octanol and water, pH 7.4, was determined by measuring the absorbance at the Soret band of the two phases after equilibrium was reached. Using equal volumes of the system phases containing 50% 1-octanol and 50% water pH 7.4 [23] carried out 1-Octanol-water partitioning. 40 μM of the dyes were added to a mixture of 1.16 ml water and 0.16 ml 1-octanol. The solution was kept at 4° C for 30 minutes, properly mixed and then stored at 37° C overnight to allow a complete separation of the phases. The concentrations of the dyes in the phases were determined spectrophotometrically and the partition coefficient calculated.

2.6. Singlet escited states lifetimes calculation

The singlet lifetime (radiative lifetime) of the riboflavin was calculated with an integration method, ruled on an ATARI computer. The formula used was that given by Bowen and Wokes.

$$1/\tau_r - 2900\ n^2\ \nu_o^2\ \varepsilon\ d\nu\ (\tau_r \text{ in s}) \qquad (1)$$

where $\varepsilon\ d\nu$ is the area under the curve of molar absorption coefficient plotted against wavenumber ;

ν_o is the wavenumber of the maximum of the absorbtion band ;

n is the refractive index of the solvent.

3.RESULTS AND DISCUSSION

3.1. Absorption and fluorescence spectra

It is known that porphyrins aggregate and these aggregates have a low fluorescence quantum yield compared with monomers [24]. Therefore, a difference between the absorption spectra and the fluorescence excitation spectra of such dyes is indicative as partial aggregation. The absorption spectra and the fluorescence excitation and emission spectra are significantly different for most of the dyes tested in this area. The specific values are shown in Table 1. Molecular aggregation has been shown to broaden the absorption bands of porphyrins and to reduce the corresponding molar absorption coefficients.

Table 1.

Spectral properties and data for partitioning coefficients of the drugs.

Drug	absorption	excitation	fluorescence (λ_{ex} = 427 nm)	phosphorescence (λ_{ex}= 427 nm)	partition coefficient
C2AITSPP	215; 230; 263; 266; 432; 570; 603; 645; 827	236; 254; 300; 330; 368; 438; 564; 644	344; 425;588; 651; 676;708; 854;	950; 1075	0.23
C8AITSPP	212; 222; 264; 428; 564; 606; 645	250; 300; 422; 564; 608	426; 598; 652 826; 706; 776;	950	0.37
C12AITSPP	212; 222; 264; 428; 564; 606; 645	442; 644	426; 598; 652; 856	1075	0.32

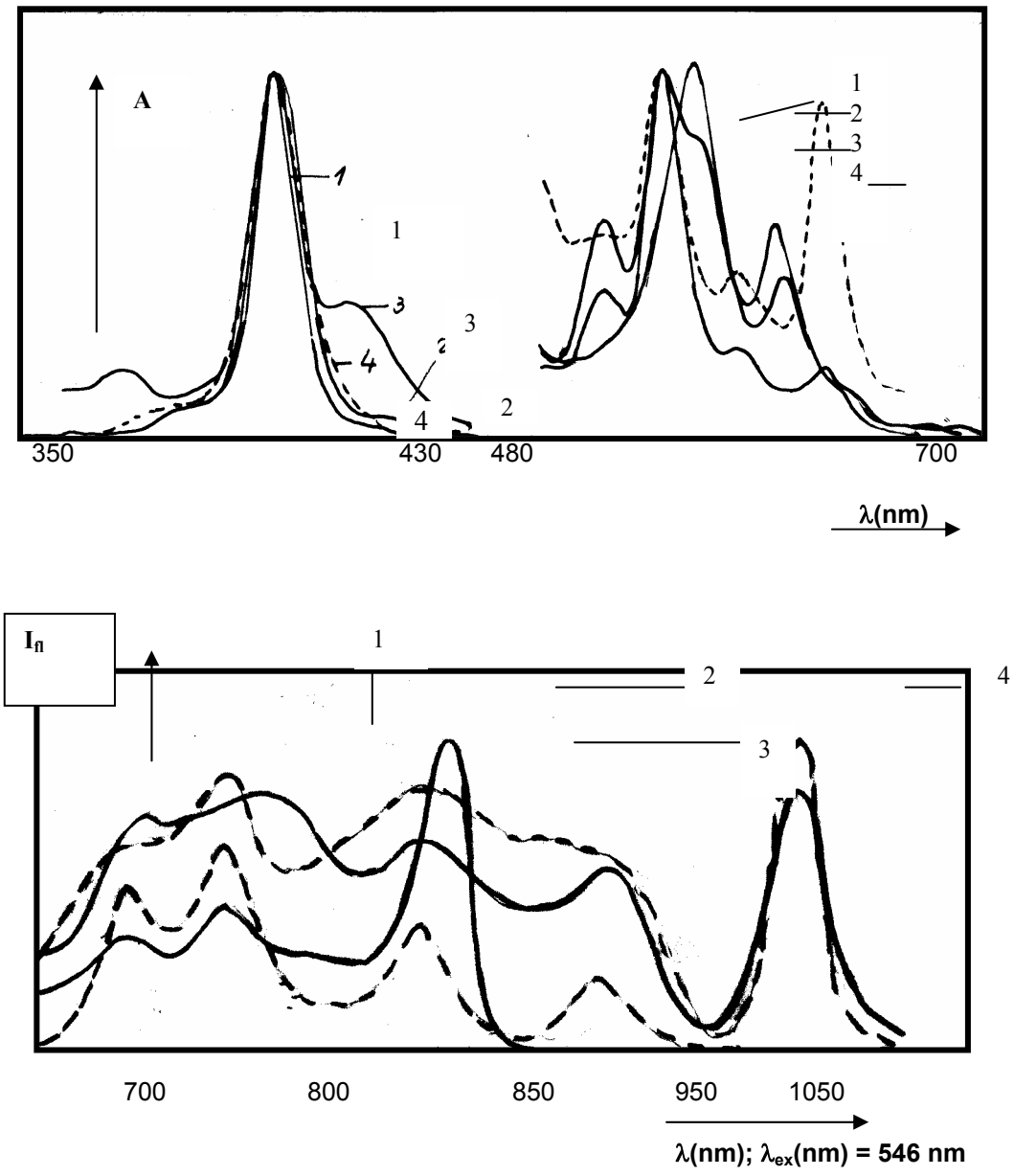

Fig. 2. The absorption and fluorescence spectra of all Al- porphyrins in DMSO solvent.
1-C2AlTSPP; 2-C4AlTSPP; 3-C8AlTSPP; 4-C12AlTSPP

By analyzing this table, could be observed that the absorption spectra have larger bandwidths than the fluorescence excitation spectra. This indicates that the cells take up aggregates as well as monomers, in good agreement with the other literature data [6]. It is very important to observe that all the cell bound dyes show a peak in their excitation spectra in the range 260-295 nm, corresponding with the excitation peak of protein fluorescence (detected for the emission λ=350 nm) and being attributed to an energy transfer from proteins to the dyes [25] (responsible for a short distance between cell bound dyes and tryptophan residues in proteins).

The emission spectra of the tested cell-bound dyes are shown in Fig.2. Usually, the cell inactivation by aluminum porphyrins is not correlated with the absorption of cell-bound aluminum porphyrins at 612 nm, but much better with the fluorescence from cell bound aluminum porphyrins.

The survival curves of EL-4 cells exposed to light after 18 h incubation with aluminum porphyrins, have an allure like in Fig.3.

This is in agreement with the observation that the action spectrum for cell inactivation follows the fluorescence excitation spectrum of different porphyrins. An action spectrum (AS) is simply defined as the measurement of a biological effect as a function of wavelength. It is possible to obtain important informations about the photoresponses of different organisms, although it may be impossible to identify either the molecule, or the mechanism involved in the process being studied.

Also, the relative fluorescence intensity from cellbound aluminum porphyrins correlates well with the amount of monomers in the cells.

For this work, we tried for the first time to evaluate the correlation between the cell inactivation by means of bleaching of DPBF.

Φin (-) is the quantum yields of cell inactivation in the absence of DPBF;

Φin(+) is the quantum yield of cell inactivation after 1 h incubation with 50 mM DPBF.

DPBF has been extensively studied as a singlet oxygen scavenger because of its high reaction constant [25]. The results are shown in Fig. 4.

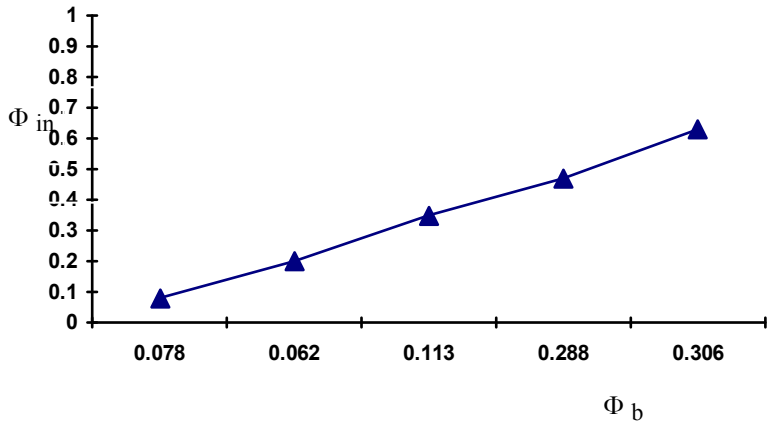

Fig.3. The correlation between the quantum yield of photodynamic inactivation of EL-4 cells and the photodegradation of DPBF

Φb is the photodegradation of DPBF in the cells, normalized to 1 for PII (protoporphyrin). For experiments of cells inactivation, the yields of the photodegradation of DPBF in cells is much faster and easier to carry out than a study of the photoinactivation yields. There is a linear relationship between Φ_b and its a certitude that knowing Φ_b could be evaluated the inactivation yield for such cells.

The quantum yield for singlet oxygen generation was evaluated in this experiments by using DPBF method [ ] coupled with FFT method which is more adequate (working for very small reaction time) for these very unstable porphyrins. Under such circumstances, the quantum yields are as is shown in Table 2.

Table 2.

The singlet oxygen quantum yields and the lifetime values for the first excited states of Al porphyrins

Porphyrin	$^1O_2$ quantum yield	Lifetime for singlet excited states of porphyrins (ps)
C2Al TSPP	0,96	5.03
C4AlTSPP	0.78	40,8
C8AlTSPP	0.83	32,9
C12AlTSPP	0.665	47,5

All these values are in good agreement with the lifetime values for the first singlet excited states of these porphyrins. An example for this experiments is shown for C2AlTSPP, Fig.5.

The partition coefficient between octanol-1 and water pH 7.5 was determined by measuring the absorbance at the Soret band of the two phases, after equilibrium was reached. The cellular uptake of different drugs seems to be correlated to their hydrophobicity only when the drugs are very closely related in chemical structure. Aluminum ion has a great influence on the sensitizer hydrophobicity without a corresponding effect on the cellular uptake.

Table. 3.

The data for cellular uptake of the drugs

Porphyrin	$K_{octanol}$
TSPP	0.47
C2AlTSPP	0.23
C8AlTSPP	0.37
C12AlTSPP	0.32

Nevertheless, the porphyrin with C2 is not as well uptaken as TSPP, even in the studied series this porphyrin is the most reactive. So, probably this porphyrin is the best recommended for such experiments.

The obtained data should not be regarded to prove that singlet oxygen is the only cytotoxic photoproduct involved in this process.

The uptake ratio of porphyrins in vitro increase when increasing the lipophilic property of the drug. The uptake of aluminum porphyrins increases linearly with increasing lipophilicity.

The inactivation kinetics for EL-4 cells is shown in figure 6.

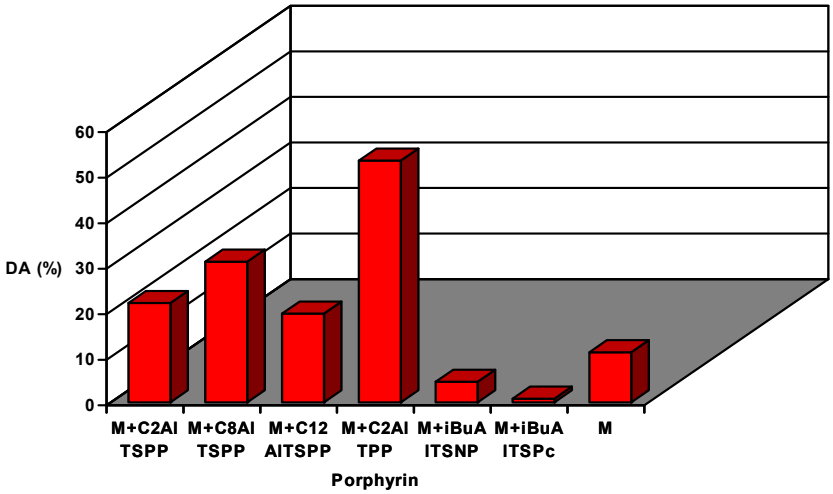

Fig.4. The inactivation diagram for EL-4 cells with aluminum porphyrins

The parameter ΔA(%) has the meaning of the absorbance decreasing of the cellular suspension (A-Ao)/Ao during PDT treatment.

4. CONCLUSIONS

Several parameters for porphyrin dyes, used as sensitizers for PDT aluminum porphyrin tetrasulphonate with different axial ligands C2, C4, C8 and C12, are evaluated in this paper, as follows:

- absorption, fluorescence-excitation and fluorescence-emission spectra of the cell-bound dyes;
- relative quantum yields for photoinactivation of EL-4 cells (prelevated from singenic mice C57 Bl/6) after 18 hours incubation with the dyes;
- relative quantum yields of photodegradation of the singlet oxygen trap-1,3-diphenylisobenzofuran (DPBF) in cells after 18 h incubation with the dyes;
- data processing with Fast Fourier Transform for singlet oxygen quantum yield;
- partition coefficients in 2-octanol-water system.

All these experiments provided us new and interesting results concerning the photodynamic inactivation of EL-4 cells as model for subsequently human cells. It's more efficiently the aluminum porphyrins with axial ligand wearing a shorter chain than one with a longer chain. This rule is valid until C8 ligand, because increasing the chain, the activity will decrease.

REFERENCES

1. D. P. Valenzeno, M. Tarr, Mechanisms of cellular photomodifications, *ACS Symp Ser., 616, 24-32(1995);*
2. R. M. Ion, Photodynamic therapy-a photocatalytic or a photosensitization process? *Progr.Catal., 6(1)55-64(1997);*
3. R. M. on, *Virtual IUPAC Photochem. Symp.: http://www.chm.tu-dresden.de/photoiupac2000;*
4. R. M. Ion, Porphyrins for tumor destruction in photodynamic therapy, *Curr.Topics Biophys., 24(1)30-42(2000);*
5. R. M. Ion, Porphyrins for photodynamic therapy of human brain tumors, *Bull.Chem.Brain, accepted 2001;*
6. R. M.Ion, A. Planner, K. Wiktorowicz, D. Frackowiak, The incorporation of various porphyrins into blood cells measured via flow cytometry, absorption and emission specroscopy, *Acta Biochim.Pol., 45(3)833-7845(1998);*
7. M. L. Pascu, L. Danaila, R. M. Ion, A. Popescu, M. Pascu, Photodynamic therapy studies on brain tumors using N2 pulsed lasers, *Proc SPIE, 4166,140(2000);*
8. G. Oenbrink, P. Jurgenlimke, D. Gabel, Accumulation of porphyrins in cells: influence of hydrofobicity, aggregation and protein binding, *Photochem.Photobiol., 48(4)451(1988);*
9. R. M. Ion, C. Mandravel, The photodegradation reaction of some porphyrins, *South Braz.J.Chem.Soc., V(5)111-129(1997);*
10. R. M. Ion, The photodegradation reaction of TNP, *Rom.J.Biophys., 8(3)219-230(1998);*
11. R. M. Ion, M. Grigorescu, F. Scarlat, A. V. Niculescu, V. I. R. Niculescu, K. Gunaydin, The aggregation and photodegradation of TNP in radiation fields, *Rom.Rep.Phys, 52(8-9)2000;*
12. T. S. Mang, T. J. Dougherty, W. R. Potter, D. G. Boyle, S. Somer, J. Moan, Photobleaching of porphyrins used in photodynamic therapy and implications for therapy, *Photochem.Photobiol., 45(4)501-506(1987);*
13. W. M. Sharman, C. M. Allen, J. E. Van Lier, Photodynamic therapeutics: basic principles and clinical applications, *Curr.Trends Drug.Discovery Today, 4(11)507-517(1999);*
14. D. Frackowiak, A. Waszkowiak, R. M. Ion, K. Wiktorowicz, I. Cofta, H. Manikowski, The interaction of phthalocyanines with stimulated and resting human peripheral blood mononuclear cells, *Acta Biochim.Pol., accepted 2001;*
15. F. H. Moser, A. C. Thomas, in *Phthalocyanine compounds, Reinhold New York, 1963;*
16. M.Gouterman, in D.Dolphin,(ed.) *The porphyrins, Vol.III, Acad.Press, New York, 1978,p.1;*
17. R. M. Ion, C. Mandravel, Spectroscopic properties of aluminum porphyrins, *Bulg.Acad.Chem.Soc.,*
18. R. M. Ion, Rom.J.Biophys.,
19. W. P. Drake, P. C. Ungaro, M. R. Mardiney, Passive administration of antibody and complement in producing anti EL4 cytotoxic activity in the serum of C 57 Bl/6 mice, *J.Natl.Cancer Inst., 50, 909(1973);*
20. O. Takahide, T. Mikio, K. Hiroyuki, F. Hiroshi, O. Shizuo, Isolation and deactivation of a low metastatic variant from EL4 mouse T lymphoma, *Clin.Exp.Metastasis, 10, 297-308(1992);*
21. J. W. Coooley, J. W. Tuxey, An algorithm for the machine calculation of complex Fourrier Series, *Math. Computation 19, 97(1965);*

22. A. V. Oppenheim, R. W. Schafer, Digital Signal Processing, Prentice-Hall, Englewood Cliffs, N.Y., 1975;
23. R. M. Ion, Accumulation of porphyrin drugs in cells. Chemical and biochemical criteria. *Proc.1-st Symp. Drug research between information and life sciences,p.6(1996);*
24. R. M. Ion, J. Moan, A. I. Vistnes, Porphyrin photosensitization of proteins in cell membranes as studied by spin-labelling and by quantification of DTNB-reactive SH-groups, *Photochem.Photobiol., 44,15(1986);*
25. I. B. C. Matheson, J. Lee, B. S. Yamanishi, M. L. Wolarsht, Measurement of the absolute rate constants for singlet molecular oxygen reaction with 1,3-diphenylisobenzofuran, and physical quenching by ground state oxygen, *J.Amer.Chem.Soc., 96, 3343(1974);*

STUDIA UNIVERSITATIS BABEŞ-BOLYAI, PHYSICA, XLVIII, 1, 2003

FT-RAMAN AND SURFACE-ENHANCED RAMAN STUDIES OF POTASSIUM-BENZYLPENICILLIN

T. ILIESCU[1]

ABSTRACT. FT Raman spectrum of potassium-benzylpenicillin (PBP) solid state and normal Raman spectrum of its solution were recorded in order to put in evidence some change of molecucular structure. The vibrational modes were assigned by comparison with infrared spectrum of PBP. Surface-enhanced Raman spectrum of PBP in silver colloid was also recorded and compared with Raman spectrum of its solution. Was found that PBP molecule is absorbed through carboxylate group on silver surface. Thiazolidine and beta-lactam groups were found to be oriented approximately parallel to metallic surface. The amide group is tilted oriented with respect metalic surface. Benzene ring is not bonded direct to the surface and is oriented perpendicular to it. The electromagnetic mechanism plays an important roll in the enhancement of the Raman bands of PBP.

Introduction

Benzypenicillins are the components of the big family of antibacterial drugs. Their biological activity is due to presence of the beta-lactam-thiazolidine ring system, common to all penicillin's (Fig 1). X-ray study of PBP [1] confirms non-planar conformation of this molecule as can be seen in the figure 1. Dziengelewski *et al*. [2] performed some vibrational studies on BP. Also Reipa and Horvath studied the adsorption of sodium-BP on silver electrode in electrochemical cell at certain potential [3].

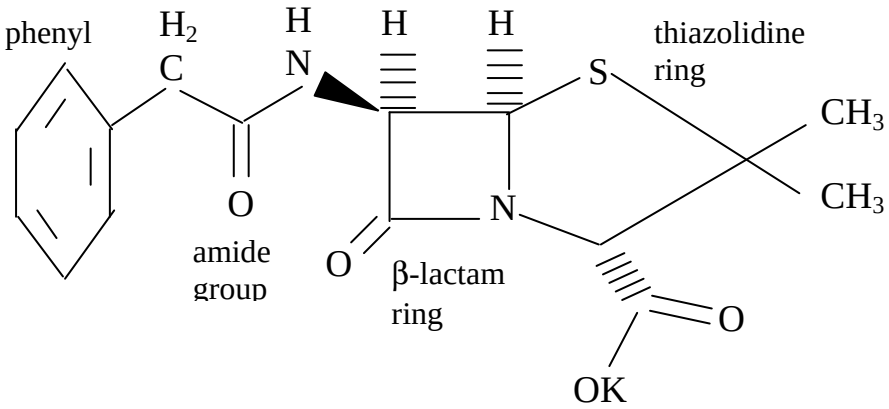

Fig. 1. Structural formula of potassium-benzylpenicillin

[1] *Babes-Bolyai University Physics Faculty, Kogalniceanu 1, 3400 Cluj-Napoca Romania*

The study of the interaction between metals and antibiotics is important because metals have a strong influence upon the susceptibility of bacteria to penicillin in vitro [4]. No consistent Raman data are available in the literature on PBP.

The following aspects are interesting to be studied:

(a) if the structure of PBP molecule is the same in aqueous solution as in solid state;

(b) the adsorption of PBP molecule on silver surface.

Surface-enhanced Raman spectroscopy (SERS) [5,6] is very sensitive spectroscopic technique to study the adsorption of different molecular species on metallic surfaces. The origin of the enhancement of Raman scattering cross section at rough surfaces has been an active field of research. Its now widely accepted that there are two main contributions to the overall SERS effect. an electromagnetic contribution and chemical effect [5,7]. The electromagnetic mechanism of the Raman enhancement is based on the increase of the electric field intensity near the metal surface due to the resonance plasmon excitation. This effect is not dependent of the specific interaction between the molecules and the metal but is strongly related to the large-scale roughness that characterized the substrate surface [5]. In the short-range chemical or charge-transfer mechanism, a modulation of the molecule's electronic polarizability arising from the interaction with the surface is responsible for the enhancement, and chemical nature of the molecules become important [7,8]. In order to assign the vibrational modes and to know if molecular structure of PBP is the same in aqueous solution as in solid state we recorded and analyzed FT Raman spectrum of PBP solid state and conventional Raman spectrum of its solution. We also recorded and analyzed SER spectrum of PBP adsorbed on silver colloid to determine the linkage of this molecular specie on silver surface.

Experimental

PBP was purchased from Terapia Cluj-Napoca factory. FT Raman spectrum was recorded using Brüker IFS 120HR spectrometer with an integrated FRA 106 Raman module and resolution of 2 cm^{-1}. Radiation of 1064 nm from Nd-Yag laser was employed for excitation. SER spectrum and conventional Raman spectrum of PBP aqueous solution were recorded using GDM 1000 double monochoromator, 514.5 nm and 200 mW out put of Innova 90 argon ion laser. 90^0 geometry was used to collect the scattered light. The detector of the Raman signal was carried out by photoelectric detection and processed by computer with some home interface. Sodium citrate silver colloid, prepared according to the literature [9] was used as SERS substrate. In order to avoid the decomposition, PBP aqueous solution was used immediately after preparation. A 5.10^{-1}mol L^{-1} solution was used to record conventional Raman spectrum. A small amount of PBP 3.10^{-1} aqueous solution was added to 2mL colloid. 0.2 mL 10^{-1} mol L^{-1} KCl solution was added for producing a considerable enhancement of the SER spectrum. The final concentration of the sample was approximately 3.10^{-2} mol. L^{-1} and pH value of 6.5. All measurements were made at room temperature.

Results and discussion

FT Raman of PBP solid state and aqueous solution spectrum are presented in figure 2 and 3 for spectral range 500-1800 and 2800-3500 cm^{-1} respectively. Table 1 presents Raman and SERS wavenumber at the pH value of 6.5. The assignment of the normal modes was performed by comparing our data with results obtained by Dzeingelewski et al. [2] from infrared spectrum of PBP and Raman spectrum of natrium-benzylpenicillin [3].

As can be seen in the figure 1 the following groups are present in PBP structure: amide group, beta-lactam, thiazolidine and phenyl rings. We will discuss the assignment of the vibrational modes by considering these groups.

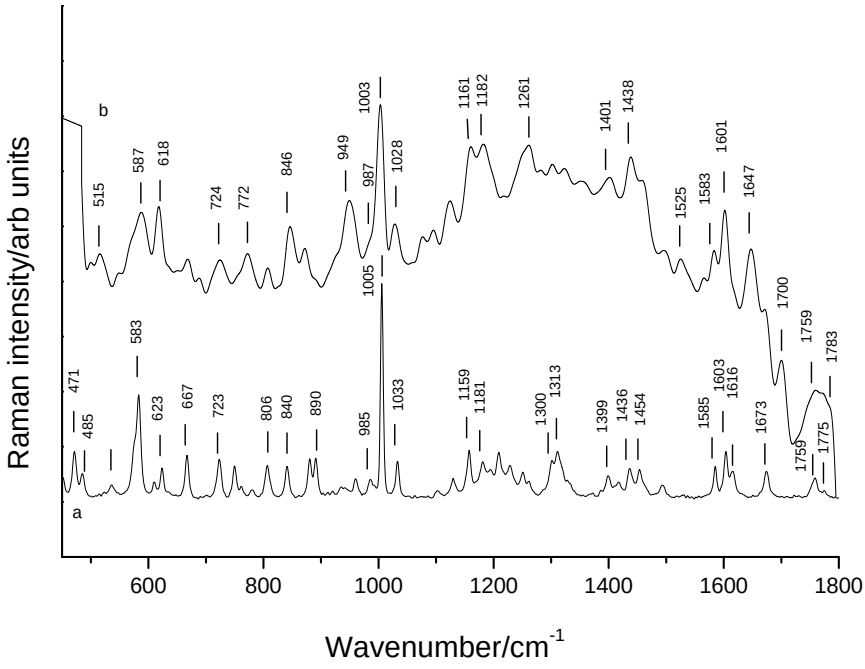

Fig. 2. FT Raman solid state (a) and normal Raman spectra (b) of potassium-benzylpenicillin solution (500-1800 cm^{-1}). Excitation lines: 1064 nm of Nd-YAG laser for FT Raman and 514.5 nm of argon ion laser for Raman of solution

(A) Vibrational analysis

Amide group vibrations

The amide group is the main constituent of complex amides and peptides. Secondary amides, like amide group in PBP, present two cis and trans conformers:

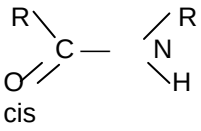

cis

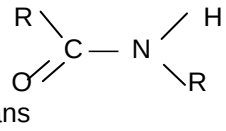

trans

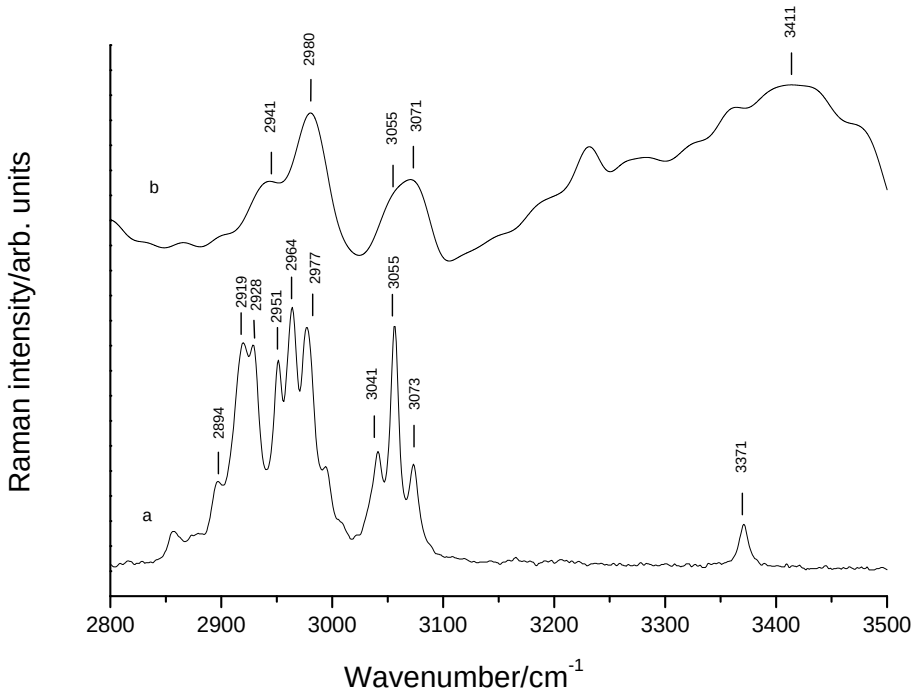

Fig. 3. The same as in Fig. 2 in the range of 2800-3500 cm^{-1}

Table 1.

Raman solid state, solution and SERS wavenumber at pH value of 6.5 of potassium-benzylpenicillin and their assignment.

[a]Abreviations:s-strong, w-weak, v-very, m-medium, sh-shoulder

FT Raman solid state cm^{-1}	Raman solution pH 6.5 cm^{-1}	SERS pH 6.5 cm^{-1}	Assignment
515(m-w)[a]	515(m-w)		Amide VI
536(vw)	549(vw)	542(w)	C-C-O in-plane def.
583(s)	587(m)	589(w-m)	CSC sym. stretch.
623(m)	618(m)	612(w)	Amide IV + in-plan def. benz. ring
667(w-m)	668(w)	670(vw, sh)	CSC asym. bend..
724(w-m)	724(w-m)	724(w)	O-C=O in-plane bend.
745(w)			CH out-of –plane benz. ring
771(vw)	772(w-m)	768(w-m)	CH_3 wagging
806(w)	807(w)	801(m)	
840(vw)	846(w)	835(m)	out-0g-plane def. benz. ring
880(w-m)	871(w-m)	860(sh)	CH_3 rock.
890(w-m)	890(sh, vw))	906(w)	CH_3 rock.
960(vw)	949(m)	942(vw)	CC stretch. beta-lactam ring
986(vw)	989(sh)		ouy-of-plane CH def. benz. ring
1005(vs)	1003(s)	1001(m)	benz.ring breathing
1033(w-m)	1028(w-m)	1025(w)	CH in-plane def.
1103(w-m)	1095(w)		
1130(vw)	1124(m)	1112(w-m, br)	CC stretch.
1159(w-m)	1161(m)	1153(m)	C-CH_3 rock.
1181(w)	1182(m)	1170(m)	CH in-plane bend. benz.ring
1211(w)	1215((vvw)	1216(w)	CN stretch. thiazolid. +beta lactam rings
1250(w-m)	1250(sh)	1252(w)	NCN in-plane bend. beta-lactam ring
1300(sh)	1302(vw)	1284(w)	Amide III trans-form
1313(w-m)	1322(vw)	1316(w, sh)	Amide III cis-form
		1382(vs)	carbon layer contribution
1399(w)	1401(w-m)	1404(sh)	COO^- sym. stretch.
1417(vw)(w)			CH_3 sym. def.
1436(v-m)	1438(m)	1428(sh)	CC stretch. benz. ring
1454(w)	1457(w)	1451(sh,w)	CH_3 asym. def..
1585(w-m)	1583(w)	1559(s)	Amide II
1603(m)	1601(m)	1587(s)	COO^- asym. stretch..
1616(w)	1617(sh,w)		benz. ring stretch.
1673(w-m)			
	1759(m)		C=O stretch.

11673(w-m)	1671(sh, w)		Amide I
	1781(sh,w)		C=O stretch. beta-lactam ring
1759(w)	1759(m)		C=O stretch. carboxyl group
	2914(w)	2904(vw)	CH_2 sym. stretch.
1775(vw)	1783(sh, w)		C=O beta-lactam ring.
2894(w)	2896(vvw)		CH_3 stretch..
2919(s)			CH_2 stretch.
2951(s)	2941(w)		CH_3 asym. stretch.
3055(s)	3055(w)	3050(vw)	CH stretch. benz. ring
3073(w)	3071(w-m)		CH stretch. beta-lactam+thiszolid. rings
3371(w)	3494(vw)		NH stretch.

The nitrogen-hydrogen stretch vibration of secondary amides is located near 3300 cm^{-1} in the associated state; for nonbonded state the same vibration is at 3491-3421 cm^{-1} for trans-form and at 3440-3404 cm^{-1} for cis-form [10]. In FT Raman of PBP solid state a band at 3371 cm^{-1} is present in this spectral range, which confirm the presence of hydrogen bond between carboxyl oxygen and amide nitrogen (N-H...O=C). Solution Raman spectrum presents too a broad band at 3411 cm^{-1}.

According to Dexter and van der Veen [11] the amide group in benzylpenicillin has trans configuration.

The Amide I band (mainly attributed to the C=O stretching mode –70-80 %; however the C-N stretching –30-10 % and N-H bending-20-10 % modes also contribute) for trans-form of N-monosubstituted amides is located at 1680-1630 cm^{-1} in solid state and in the range 1700-1650 cm^{-1} in diluted solution [10]. The cis-form has also its Amide I band in this region.

In FT Raman spectrum of PBP solid state and in solution a band at 1673 cm^{-1} and respectively at 1671 and 1700 $cm^{-1}$are present. Reipa and Horvath detected no band in Raman spectrum of natrium-benzylpenicillin solid state in this spectral region [3].

Amide II bands (the major contribution is from N-H bending mode but the contribution of C-N stretching exist) are located around 1570-1510 cm^{-1} for trans associated form and around 1550-1500 cm^{-1} in the free form. No Amide II band is found in this region for cis configuration [10].

In FT Raman spectrum of PBP only a band at 1585 cm^{-1} exist which have the corresponding band at 1583 cm^{-1} in Raman spectrum of solution. In Raman of solution the bands at 1565 and 1525 cm^{-1} also exist.

The interaction of the N-H bending and C-N stretching (the contribution of both vibrations being approximately the same) also produces another characteristic frequency called the Amide III band which in liquid and solid (associated) states is found at 1330-1250 cm^{-1} and in the free state is locates at 1250-1200 cm^{-1} [10]. In FT Raman solid state and in solution of PBP in this range are present the bands at 1313 and 1300 cm^{-1} and at 1322 and 1302 cm^{-1} respectively. First bands (1313 and 1322 cm^{-1}) are assigned to the cis-form and the second bands (1300, 1302 cm^{-1}) are determined by trans-form.

Another characteristic band in substituted amide is near 630 cm^{-1} in amides of the type R-CH_2-CO-NHR [10]. This is called the Amide IV band and arises principally from the O=C-N bending mode. In FT Raman as in solution spectra of PBP a band at 623 cm^{-1} and 618 cm^{-1} respectively is present. The Amide V band (N-H out-of-plane bending) and the Amide VI band (C=O out-of-plane bending) generally appears as very weak lines in the Raman and do not lead to the useful correlation.

From X-ray study [1] was concluded that amide group have trans-form in solid state of PBP because this configuration assures the hydrogen bonding between carboxyl oxygen and amide nitrogen. Miyazawa [12] concluded from infrared spectra that cis-form Amid I and Amid III bands are located at high frequencies while the Amide II band is observed at low frequencies by comparison with the same bands for trans conformer. The conformers frequencies difference was found to be 40 cm^{-1} for Amide I, 100 cm^{-1} foe Amide II and 50 cm^{-1} for Amide III bands.

In Raman spectra of PBP was observed a deviation from these differences providing the conformation change of this group.

Monosubstituted benzene ring vibrations

According Dollish et al. [10] a monosubstituted benzene ring can be identified in the Raman by intense band at 1000 cm^{-1} determined by ring breathing vibration, a shoulder at 995 cm^{-1} which correspond to the out-of-plane CH deformation, a medium band near 1028 cm^{-1} derived from the vibration 18a in-plane CH deformation of benzene ring. Weak band near 618 cm^{-1} characteristic to the benzene ring deformation and derived from vibration 6a (606 cm^{-1}) of benzene, two weak bands near 1170 cm^{-1} obtained from e_{2g} benzene vibrations (9a and 9b), a doublet obtained from vibrations 8a and 8b (e_{2g}) (benzene ring stretching) and CH stretching band near 3060 cm^{-1} also exist in monosubstituted benzene.

As can be seen in Fig. 2a a strong band is observed around 1003 cm^{-1} with the shoulder at 985 cm^{-1} in FT Raman and 987 cm^{-1} in Raman of solution. In-plane CH deformation is present at 1033 cm^{-1} in FT Raman and 1028 cm^{-1} in solution. In-plane deformation mode of benzene ring is present at 623 cm^{-1} in solid state Raman spectrum. Is very difficult to assign this band because in mentioned spectral range have the contribution from the Amide IV band. In-plane CH deformation is present as a doublet at 1181, 1193 cm^{-1} in FT Raman and 1182 and 1200 cm^{-1} in Raman of solution. The doublet near 1600 cm^{-1} (benzene ring stretching 8a, 8b) was very difficult to assign because in this region the contribution from asymmetric stretching mode of COO^- group also exist. However a band at 1616 cm^{-1} is present in FT Raman and a shoulder at 1617 cm^{-1} in solution. CH stretching band is observed at 3055 cm^{-1} in FT Raman and 3052 cm^{-1} in solution (Fig.3)

CH_3, CH_2, and CH group frequencies

The vibrations of these groups are present in Raman spectra of PBP as follows: $\nu_{as}(CH_3)$-2951 cm^{-1}, $\nu_s(CH_3)$, $\nu_s(CH_2)$ at 2894 and 2914 cm^{-1} (Fig.3a). Raman spectrum of solution presents in this region very broad bands at 2941, and 2980 cm^{-1}. Ther CH_3 asymmetric and symmetric deformation are present in FT Raman solid state of PBP at 1454 and 1417 cm^{-1}. The C-CH_3 and CH_3 rocking vibrations can be identified in FT Raman at 1159 and 890 cm^{-1}. In soluition Raman spectrum the corresponding bands are observed at 1457, 1161 cm^{-1} and very weak shoulder at 890 cm^{-1} (Fig.2a).

Carboxyl group vibrations

In-plane deformation of the O-C=O group is present in FT Raman of solid state and solution of PBP at the same value of 724 cm^{-1}. The band at 536 cm^{-1} in FT Raman and 549 cm^{-1} in solution can be assigned to the in-plane deformation of C-C-O group. Symmetric stretching $\nu_s(COO^-)$ and antisymmetric stretching $\nu_{as}(COO^-)$ are present in FT Raman and in solution spectra as weak band at 1399 cm^{-1} and 1603 cm^{-1} and 1401 and 1601 cm^{-1} respectively. A medium-intense band at 1759 cm^{-1} in FT Raman and solution can be assigned to ν(C=O) of carboxyl group. The same vibration is present in IR spectrum of PBP at 1754 cm^{-1} [2].

Beta-lactam (ε) and thiazoilidine (ζ) ring vibrations

The conjugation between these two rings is reflected in the vibration of atoms. The C=O stretching mode in beta-lactam was found [2] to be located at 1770-1780 cm^{-1}. The other stretching of these rings are present in IR spectrum of PBP [2] on the following ranges: ν_ε(C-C), ν_ε(C-C), ν_ε(C-N), ν_ζ(C-N) at 1215-1180, 1072-1132, and 910-990 cm^{-1}. The deformation vibrations δ_ε and δ_ζ of these systems, that is δ(CCN), δ(CNC), δ(CCC) are present at the low frequencies than 450 cm^{-1} [2].

In FT Raman spectrum of PBP the very weak band is observed (see Fig.2a) at 1775 cm^{-1} and the shoulder at 1783 cm^{-1} in solution. We assign this band to the ν_ε(C=O) vibration. The CN stretching mode in tyazolidine and beta-lactam rings is observed at 1221 cm^{-1} in FT Raman. NCN in-plane bending mode of beta-lactam ring is present in FT Raman by the band at 1246 cm^{-1} and 1250 cm^{-1} in Raman spectrum of solution. The strong band at 583 cm^{-1} in FT Raman and 587 cm^{-1} in solution is assigned to the symmetric stretching of the group CSC of thiazolidine ring. The asymmetric stretching ν_{as}(CSC) is present in Raman of solution at 667 cm^{-1}.

By comparison of the FT Raman and Raman spectra of PBP solution presented in the figure 2 and 3 we observe that:

(a) The bands in solution are more broadened than in FT Raman of solid state. This situation is determined by stronger molecular interaction in liquid than in solid state.

(b) Relative intensities of the bands and relative position of some of them a different in solution than solid state spectrum; the strong changes are visible on the beta-lactam and thiazolidine ring bands.Thus in solid state the dominant is the band of 1005 and 583 cm^{-1} assigned to benzene ring breathing and CSC group stretching. In solution the 1003 cm^{-1} band are still dominant band but the CSC stretching is shifted to 587 cm^{-1} an have the medium intensity. The band at 668 cm^{-1} in spectrum of solution assigned to the CSC stretching, have weaker intensity than corresponding band at 667 cm^{-1} in solid state spectrum.

The same changes were obsrved in the bands from the specral range 1170-1250 cm^{-1}.

These observation show that some changes occur into the beta-lactam and thiazilidine ring in solution. Gensmantel et al. [13] observed the hydrolyze of benzilpenicillin in water above pH 4 into benzilpeicilloic acid by opening the beta-lactam ring. The same situation probably happen in PBP solution, which have the pH value of 6.5.

B. Adsorption of PBP on silver surface.

Because there are some changes in Raman spectrum of solution compared with FT Raman PBP solid state, we will compare SER spectrum with Raman spectrum of solution.

SER spectrum and Raman spectrum of PBP solution are presented in the figure 4 and 5 for the range 500-1600, and 2800-3100 cm^{-1} respectively.

The change in the peak positions and relative intensities of bands are observed in SER spectrum compared with spectrum of solution. The orientation of the adsorbed PBP molecule can be deduced with the use of surface selection rules for Raman scattering. Creighton [8] and Moskovits and DiLella [14] were concluded that if molecular z-axis is normal to the surface, then vibration of the adsorbed state molecules, which have a polarizability tensor component along this axis will be preferentially enhanced. Vibration having large x and y tensor component will be weaker Raman band, compared to bulk spectra. The PBP molecule has very low symmetry and all vibration have polarizability tensor component along the z-axis. Gao and Weaver [15] found that monosubstituted benzene ring modes are sensitive to the orientation of the plane ring with respect to the metal surface in terms of line positions and shapes.

The peak position of the most band in SER spectrum are shifted to low wavenumber by 5-10 cm^{-1} by comparing with the position of the corresponding bands in solution. This means a strong interaction of some of part of adsorbed molecule with silver surface, which means the chemisorption of this molecular specie on the metal surface. We will discuss the interaction and orientation of each group present in PBP molecule on the silver surface.

The Amide II band in which the major contribution is from NH in-plane bending mode, the contribution of the CN stretching being possible, present in solution Raman spectrum at 1583 cm^{-1}, in SER spectrum is present as weak band at 1559 cm^{-1}. The Amide III band (equal contribution of NH in-plane bending and CN stretching modes) is also present at 1284 cm^{-1} (se table 1 and Fig. 4). The existence of these bands in SER spectrum confirms the interaction of the amide group with silver surface which probably is tilted oriented toward surface.

Gao and Weaver [15] observed significant (~ 25 cm^{-1}) down shift relative to the bulk spectra in the 1004 and 1030 cm^{-1} bands upon the flat orientation of monosubstituted benzene derivatives on silver, due to backdonation of electron density from metal to the $\pi*$ antibonding orbitals.

The ring breathing vibration (1003 cm^{-1}) and in-plane CH deformation (1028 cm^{-1}) modes of PBP benzene ring have negligible (~2-3 cm^{-1}) shift in adsorbed state compared with bulk spectrum. This fact suggests the vertical orientation of benzene ring toward silver surface in adsorbed state. This orientation is reinforced by the absence of out-of-plane CH deformation of this ring in adsorbed state, this mode being active in FT Raman (986 cm^{-1}) and Raman of solution (989 cm^{-1}). stretching vibration spec

The ymmetric and antisymmetric stretching of COO^- group were shifted by 3 cm^{-1} from 1401 and 1601 cm^{-1}in Raman of solution to 1404 and 1587 cm^{-1} in adsorbed state. This fact confirms the existence of the interaction of carboxylate group with silver surface probably by oxigen electrons of this group.

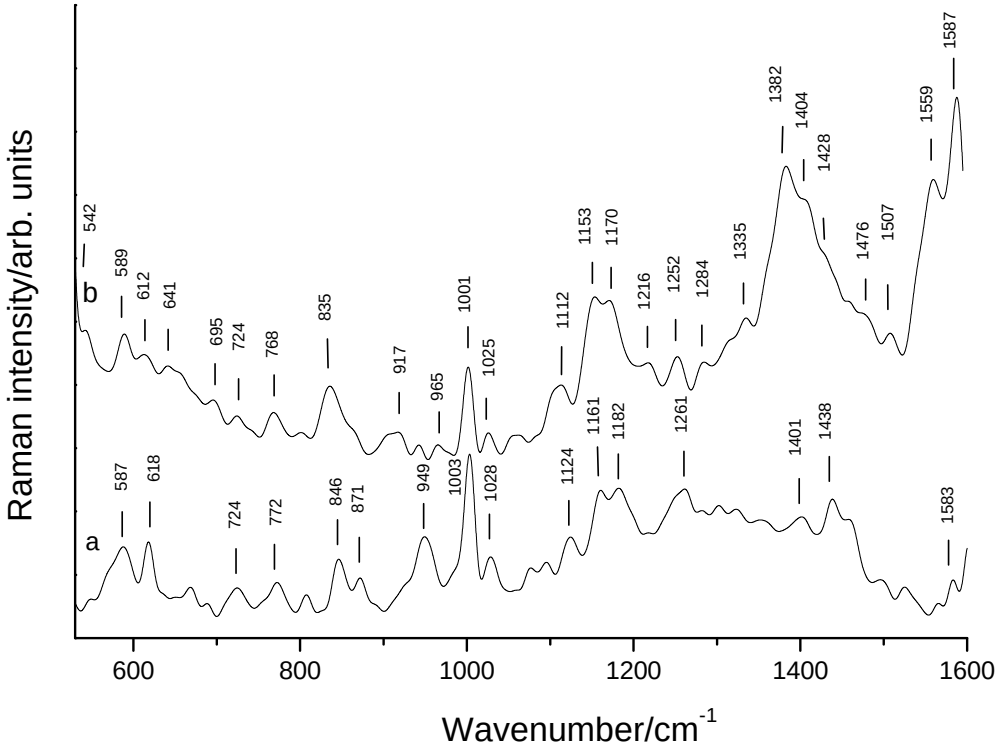

Fig. 4. Normal Raman (a) and SER spectra (b) of potassium-benzylpenicillin (500-1600cm^{1}). Excitation line:514.5 nm of argon ion laser

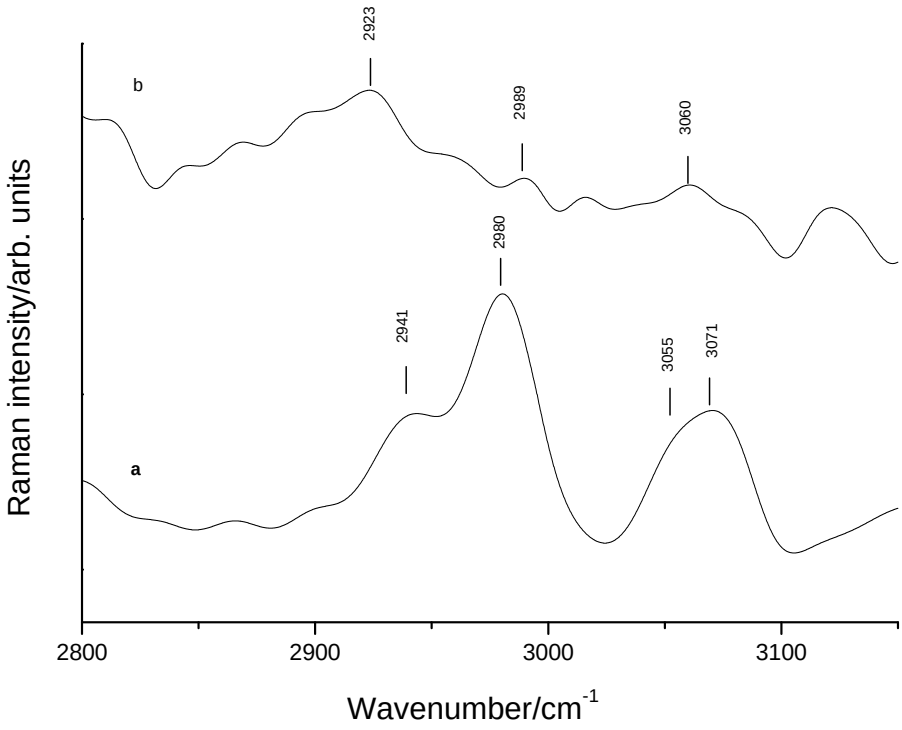

Fig. 5. The same as in Fig 4 in the range of 2800-3150 cm^{-1}

The symmetric stretching of CSC group, present in SER spectrum at 589 cm^{-1} have a negligible shift (2 cm^{-1}) compared with the corresponding band in the bulk spectrum. The antisymmetric stretching of this group present in free state at 668 cm^{-1} is still present in SER spectrum around 670 cm^{-1} as weak shoulder. This suggests that CSC group tends to become parallel toward silver surface. As Dexter and van der Veen [1] found from x-ray data, the sulfur atom is displaced 0.7 Å from the plane of the other four atoms of the thiazolidine ring, which suggest its endewise orientation toward silver surface.

We presume that the very intense and broad band present in SER spectrum at 1382 cm^{-1} is determined by carbon layer existing on the silver surface probably by the photo and thermal decomposition of PBP [16]

Conclusions

The vibrational modes were assigned from FT Raman solid state and Raman spectra of PBP solution.

The structural changes were observed in PBP molecule in solution compared with solid state. The adsorptions of PBP molecule on silver surface demonstrate surface bonding through carboxylate group. Thiazolidine and beta-lactam rings was found to be approximately parallel oriented to silver surface in adsorbed stste. Tilted orientation on metalic surface was propposed for amide group. Benzene ring was found to be aproximatelly perpendicular orientated to the surface. Because the specific frequencies of benzene ring are only negligible shift in adsorbed state compared with free state and the modes are very intense, we suppose that the contribution of electromagnetic enhancement mechanism plays an important roll in this case. Taking into account of these conclusions we suppose that in adsorbed state PBP molecule exhibit a modified structure compared to the solid-state form structure.

REFERENCES

1. D. A. Dexter, J.M. van der Veen, *J. Chem. Soc., Perkin Trans*. **1**, 185, (1978)
2. J. Dziengelewski, J. Hanuza, B. Ezowska-Trzebiatowska, Z. I. Siemion, Zh. Prikl. Spectrosk.,19, 275, (1973)
3. V. Reipa, J. J. Horvath, *Appl. Specrosc*.,**46** 1009, (1992)
4. M. Asso, R. Panossian, M. Guiliano, *Spctrosc. Lett*. **17**, 271, (1974)
5. M. Moskovits, *Rev. Modern Phys*., **57**, 783, (1985)
6. A. Campion, P. Kambhampati, Chem. Soc. Rev., 27, 241, (1998)
7. J. R. Lombardi, R. L. Birke, T. Lu, J. Xu, *J. Chem. Phys*. **84**, 4174, (1986)
8. J. A. Creighton, *Surf. Sci*., **124**, 209, (1983)
9. T. K. Lee, D. M. Meisel, J. Phys. Chem., **87**, 3391, (1982)
10. F. R. Dollish, W. G. Fateley, F. F. Bentley*, '' Characteristic Raman Frequencies of Organic Compounds*'' p.124. John Wiley and Sons, New York, London, Sydney, Toronto, 1974
11. R. M. Sweet, L. F. Dahl, *J. Am. Chem. Soc*., **92**, 5489, (1970)
12. T. Miyazawa, ''*Infrared Spectra and helical Conformation of Poly-alphaaminoacids''*. Ed. D. Fastmann, New York, 1967, p.69.
13. N. P. Gensmantel, P. Proctor, M. I. Page, *J. Chem. Soc. Perkin***, 2**, 1725, (1980)
14. M Moskovits, D. P. DiLella, *J. Phys. Chem*. **73**, 6068, (1980)
15. P. Gao, M. J. Weaver, *J. Phys. Chem*. **89**, 5040, (1985)
16. T. Iliescu, M. Vlasa, M. Caragiu, I. Marian, S. Astilean, *Vibr. Spectrosc*. **8**, 451, (1995)

STUDIA UNIVERSITATIS BABEŞ-BOLYAI, PHYSICA, XLVIII, 1, 2003

MAGNETIC PROPERTIES OF $U(Fe_xSi_{1-x})_2$ COMPOUNDS

ILEANA LUPSA[1]

ABSTRACT. The magnetic behaviour of the $U(Fe_xSi_{1-x})_2$ compounds with x=0.25, 0.5 and 0.75 was discussed The magnetic properties of U_2Fe_3Si compound reveal the spin fluctuations behaviour. The magnetic properties were discussed using the hybridization matrix elements which describe the interaction between uranium f and d and p orbitals. The total covalent energy according to the criterion of localized uranium moments is compared with the critical energy and the magnetic ordering presence may be established.

Keywords: Uranium compound; Magnetic properties; Hybridization effects

Introduction

The intermetallic uranium compounds of U_2TSi_3, UTSi and U_2T_3Si type where T is a 3d, 4d or 5d element show a wide variety of physical properties. The magnetic behaviour is determined by the uranium 5f electrons. The other components do not contribute much to the magnetic moment but influence the magnetic properties modifying the state of uranium 5f electrons. The main mechanism for delocalization of uranium 5f electrons is considered the hybridization between 5f and d electrons.

The present study follow to correlate the f-d,p hybridization potentials in the series of compounds where T=Fe with the magnetic properties.

Experimental details

The polycrystalline samples were prepared by stoichiometric amounts of the elementary metals (99.9 % purity for U and better for the others) in an argon arc furnace in a protective purified atmosphere; several times melting assured a good homogeneity.

The phase purity, the crystal type structure and the lattice parameters were determined by the standard X-ray diffraction method. The analyses indicated the presence of different crystalline structure. Starting from the USi_2 which is hexagonal of the AlB_2 type, replacing Si by Fe, the compounds present symmetry of hexagonal (AlB_2 type), orthorhombic (TiNiSi type),hexagonal ($MgZn_2$ type) and $MgCu_2$ type for UFe_2. The structural information on these compounds is collected in Table 1.

[1] *Technical University, 3400 Cluj-Napoca, Department of Physics, Str. C. Daicoviciu, nr.15, 3400 Cluj-Napoca, Romania. Email: ileana.lupsa@phys.utcluj.ro*

The compounds are not ordered except UFe_2. The susceptibility accurate values χ were determined using the Honda-Owen rule: $\chi_m=\chi+cM_s'H^{-1}$. Plotting the experimental susceptibility χ_m versus the reciprocal magnetic field, the correct susceptibility was obtained for $H^{-1} \rightarrow 0$. The influence of the possible magnetic impurity having concentration c and the saturation magnetization M_s' was in this way eliminated.

Results

The magnetic behaviour of the compounds is summarized in the Table 1. The only ordered compound UFe_2 has 1.1 $\mu_B / f.u.$ mainly due to Fe atoms. The uranium moment is 0.06 μ_B / U_{atom}. The U_2FeSi_3 present a spin fluctuations type behaviour having o constant susceptibility at low temperatures and a Curie-Weiss modified law ($\chi = \chi_0 + \frac{C}{T-\theta}$) over 30 K [1]. The UFeSi is not ordered; it has a large maximum in the susceptibility at 80 K and a Curie-Weiss paramagnetism in the high temperature range [3]. Our measurements show a Pauli paramagnet with a small variation of susceptibility vs T at low temperature region and the almost constant value of $1.59 * 10^{-3} emu / mol$. For the U_2Fe_3Si compound the field dependence of the magnetization reveals no saturation and suggests no spontaneous magnetic moments on uranium positions (Fig.1). The reciprocal susceptibility follows a modified Curie-Weiss law (Fig.2) having the negative θ values and μ_{eff} attributed only to uranium atoms. The results are collected in the Table 1.

Table 1.

Compound	Crystalline symmetry	T_C(K)	θ (K)	$\chi_0 (10^{-3} emu\ mol) / U_{atom}$	$\mu_{eff} (\mu_B / U_{atom})$	Refs.
USi_2	Hex.AlB_2	-	-386	-	3.57	[4]
U_2FeSi_3	Hex.AlB_2	-	-86	0.72	2.77	[1]
UFeSi	Orthorhombic TiNiSi	-	-2100 -	- 1.59	4 -	[2,3] present paper
U_2Fe_3Si	Hex.$MgZn_2$	-	-85	0.9	1.66	present paper
UFe_2	Cubic.$MgCu_2$	162	169	1.225	3.03	[5]

The ff, fd and fp hybridization is the mechanism of the delocalization of f electrons. This is the essential factor which determines magnetic properties in many cerium and uranium intermetallics [6]. A good estimation of the strength of hybridization may be obtained using the method suggested by Straub and Harrison [7,8,9] to determine the interactions between s,p, d and f atomic orbitals. The

evaluation of the formation of magnetic moments for a group of isostructural compounds calculates the two –center couplings between atomic orbitals of s,p,d,f symmetry. The criterion for localized magnetic moment considers the V_{total} inferior to the critical energy $U \sin^2\left(\frac{Z_f \pi}{14}\right)$ [9]. U is Coulomb repulsion and Z_f represents the number of f electrons. If V_{total} is smaller than critical energy then f electron is localized and the compound is expected to have magnetic moments. This critical energy depends on the average of f electron occupancy of uranium and is 1.38 eV and 0.68 eV for f^3 and f^2 configurations respectively.

The hybridization and covalent energy $V_{ll'}$ and V_{total} for the studied compounds are presented in Table 2 [10].

Table 2.

Compound	x	$V_{ff}(meV)$	$V_{fd}(meV)$	$V_{fp}(meV)$	$V_{total}(meV)$
USi_2	0	153	-	1478	1479
U_2FeSi_3	0.25	153	436	1279	1360
UFeSi	0.5	394	706	1239	1479
U_2Fe_3Si	0.75	719	955	762	1417
UFe_2	1	683	1054	-	1256

Discussion

The low values of V_{ff} in the compounds having x=0 and 0.25 show a small direct mutual overlap of 5f orbitals. This statement is in accord with the Hill limit criterion of the f electron localization. Large V_{fp} values suggest intense fp hybridization for the first three compounds. High V_{ff} magnitudes indicating an intense 5f-5f hybridization effects occur for U_2Fe_3Si and UFe_2. The distance d_{UU} is below the Hill limit, 2.886 Å and 3.056 Å respectively and show a high f orbitals overlap.

For the Fe richest compounds the fd hybridization effects become important. The covalent energy measured by V_{total} smaller than 1.38 eV indicates that UFe_2 is an ordered compound, presenting 0.06 μ_B / U_{atom}. The USi_2 and UFeSi are not ordered compounds with V_{total} superior to 1.38 eV. The magnetic behaviour for UFeSi as Pauli paramagnet, in accord with our measurements seems to be better ascribed by the large V_{total} value. The systems U_2FeSi_3 has V_{total} very close to that of ordered state, it present a spin fluctuations behaviour, close to the magnetic instability.

Confronting our $V_{fl'}$ values with other already published results is possible to compare the magnetic properties of UFeSi with those of UFeAl [11]. The V_{ff} in our system is superior to that for UFeAl. The hybridization fd is more intense in UFeAl and the V_{fp} values in UFeAl compounds has lower (824 meV) values than in UFeSi. This fact is expected, silicon brings two p electrons instead one electron as aluminum does.

The method developed by Straub and Harrison well estimates the intensity of f-p,d hybridization in the series of $U(Fe_xSi_{1-x})_2$ compounds except for x=0.25. For the series of UTAl compounds is also reported lower values for V_{total} for 3d group of elements [11]. The availability of the criterion concerning the magnetic moment on uranium atoms existence, show that the uranium electronic configuration is $5f^3$. More conclusions may be obtained discussing the isostructural series of compounds.

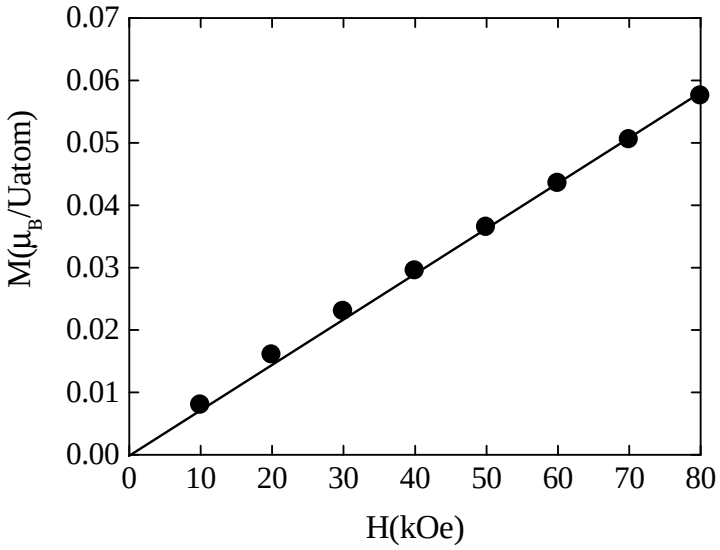

Fig. 1. The field dependence of the magnetization for U_2Fe_3Si compound

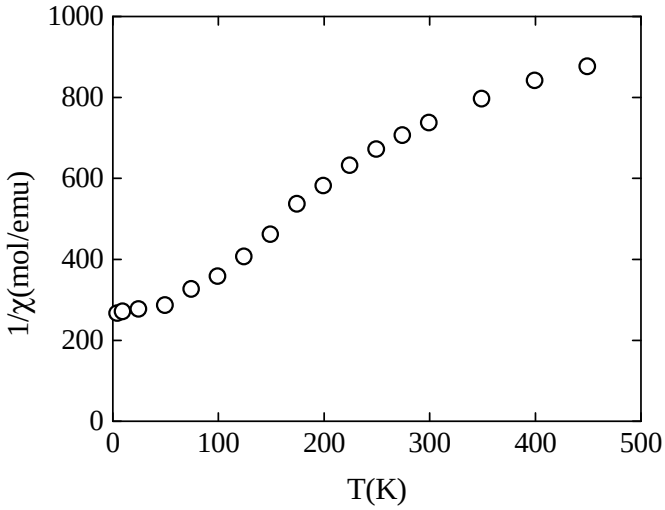

Fig. 2. The temperature dependence of the reciprocal susceptibility of U_2Fe_3Si compound

Aknowledgement

This work is part of the research program financially supported by CERES 10/2/2001 project.

REFERENCES

1. B. Chevalier, R. Pőttgen. B. Darriet, P. Gravereau, J. Etouneau, J. Alloys Compound. 233 (1996) 150
2. F. Canepa, P. Manfrinetti, M. Pani, A. Palenzona, J. Alloys Compound. 234 (1996) 225
3. A. V. Andreev, F. Honda, V. Sechovsky, M. Divis, N. Izmaylov, O. Chernyavski, Y. Homma, Y. Shiokawa, J. Alloys Compound. 335 (2002) 91
4. K.Remschnig, T.Le Bihan, H.Noël, P.Rogl, J.Solid State Chem.97 (1992) 391
5. J. J. M. Franse, R. Gersdorf, Landolt Bőrnstein III/19F1, Actinide Elements and their Compounds with other Elements, p. 117-119
6. T. Endstra, G. J. Nieuwenhuys, J. A. Mydosh, Phys. Rev. B48 (1993) 9595
7. W. A. Harrison, Phys. Rev. B 28 (1983) 550
8. G. K. Straub, W. A. Harrison, Phys. Rev. B 31 (1985) 7668
9. W. A. Harrison, G. K. Straub Phys. Rev. B 36 (1987) 2687
10. I. Lupsa, M. Valeanu, Conf. AM3, Constanta sept.2003
11. K. Prokes, E. Brück, H. Nakotte, P. F. de Châtel, F.R. de Boer, Physica B 206&207 (1995) 8

STUDIA UNIVERSITATIS BABEŞ-BOLYAI, PHYSICA, XLVIII, 1, 2003

A MECHANISTIC MODEL FOR THE ASSESSMENT OF LUNG CANCER RISK INDUCED BY RADON AND ITS PROGENY

LUCIA-ADINA TRUȚĂ-POPA*, W. HOFMANN, C. COSMA***

ABSTRACT. The present paper details a mechanistic model for the assessment of lung cancer risk induced by radon and its progeny. This mechanistic model provides risk predictions for low doses of α-irradiation, for which the extrapolation of the data for underground miners does not provide accurate assessment of lung cancer risk.

This model also estimates the resulting changes in the risk due to different parameter variations. The risk model yields, for different combinations of parameter values, approximately the same results, which are in a remarkably good agreement with the epidemiological data for the Colorado Plateau uranium miners.

Keywords: mechanistic model, assessment of lung cancer risk, radon, low doses of α irradiation, parameter variation.

INTRODUCTION

Uranium (^{238}U), a parent of ^{226}Ra and ultimately ^{222}Rn, is ubiquitous in the earth's crust. Interest in the effects of exposure to Rn has been stimulated by the recognition in the 1970s and 1980s that radon from sub soils can enter homes and accumulate there to relatively high levels, although mean indoor concentrations are substantially lower than those found in most mines. Based on estimates of risk from studies of underground miners, it has been predicted that between 6,600 – 24,000 lung cancer deaths per year in the United States may be attributable to exposure to Rn progeny [1]. Use of miner-based models for risk assessment for domestic exposure is subject to significant uncertainties, because of:

(1) differences between working miners and the general population in duration and intensity of exposure to Rn progeny and in breathing patterns;

(2) differences between the physical states of Rn and its progeny in mine and home environments, e.g., Rn equilibrium levels and the presence of differing concomitant exposures and

(3) absence of data on the effects in females and children and on long periods of exposure.

It is known that when the lungs are irradiated, epithelial cells do not experience a single value for the LET (Linear Energy Transfer) of the radon progeny α-particles, but a whole spectrum of LETs. Thus the first step of this study

* *Faculty of Physics, Babes-Bolyai University, 3400 Cluj-Napoca, Romania*
** *Institute of Physics and Biophysics, University of Salzburg, 5020 Salzburg, Austria*

was to verify whether the LET value of the α-irradiation has or has not a great importance in determining the transformation frequency for C3H 10T1/2 fibroblast mouse cells as a function of dose. For this purpose, data reported by Miller *et al.* [2] and Bettega *et al*. [3], for different LET values were used. In this study, the LET values taken into consideration were: LET = 90, 120, 150 and 101 keV/μm, for the same type of fibroblast cells. The approach in Miller and Bettega's articles was to use the *in vitro* transformation assay based on C3H 10T1/2 fibroblast mouse cells to investigate the oncogenic potential of charged particles of defined LET over a wide range of LET values. The measured data and the linear functions fitting that data are shown below:

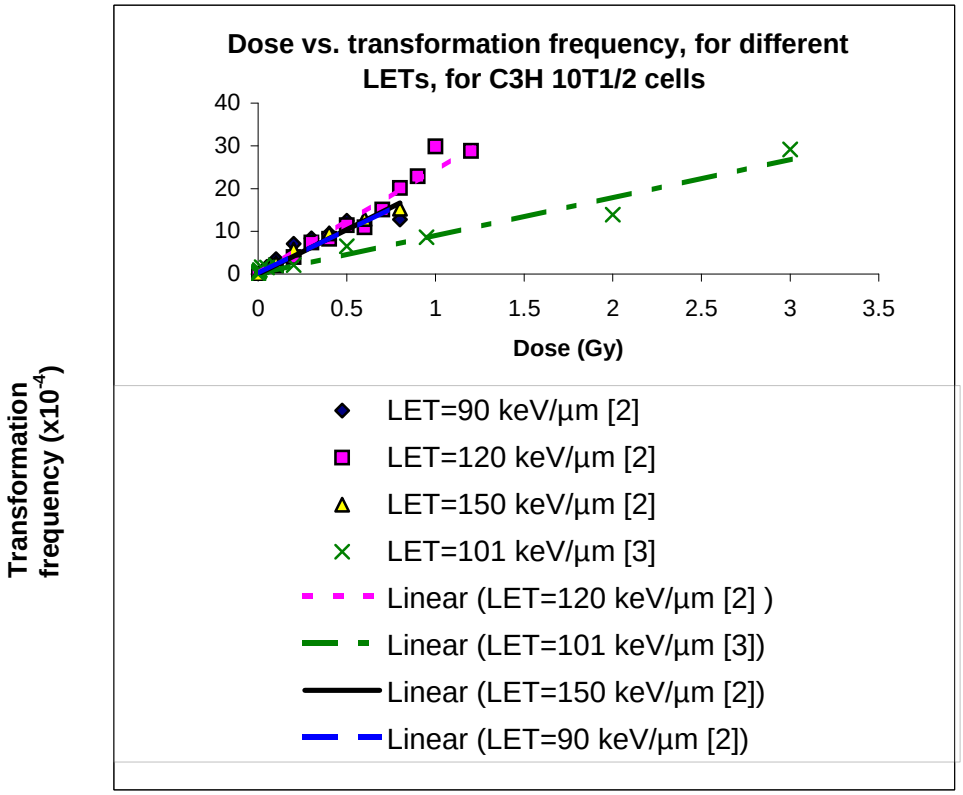

The conclusions that can be drawn from this graph are that even for different LET values, the slopes that fit the data are almost the same within a given experiment. Since there seems to be no strong dependence on LET, a single LET value for the C3H 10T1/2 mouse fibroblast cells may be used, even if in the lungs there is a spectrum of α-particles LETs. The C3H 10T1/2 cell *in vitro* transformation assay system has proven to be a valuable tool in providing quantitative data for the

risk of oncogenic transformation after exposure to alpha particles, based on past success with the excellent quantitative properties of this cell type. But the biological health effects of irradiation after the inhalation of radon and its progeny products arise from α particles reaching the secretory and basal cells in the bronchial epithelium as well as other pulmonary tissues. Given the fact that about 85% of all cancers derive from epithelial cells, a better understanding of the biological effects of α-particles on these cells must be investigated to apprehend the mechanisms of radiation-induced bronchial carcinomas [4].

For this reason, the data reported by Poncy et al. [4] for rat tracheal epithelial cells (RTE) were analyzed and compared with the data for C3H 10T1/2 fibroblast mouse cells. The aim of this comparison was to find out a factor that makes the two sets of data for the two cell types compatible. In the article of Poncy et al., primary cultures of tracheal epithelial cells obtained from two rat strains, Sprague Dawley (SD) and Wistar Furth / Fischer F344 (WF/Fi) rats, were irradiated with ^{241}Am α - particles. The primary goal of that study was to see whether the transformation induced by α irradiation in the same cell type depends on the specific strain of the rat. The results appear quite clear in the corresponding graph:

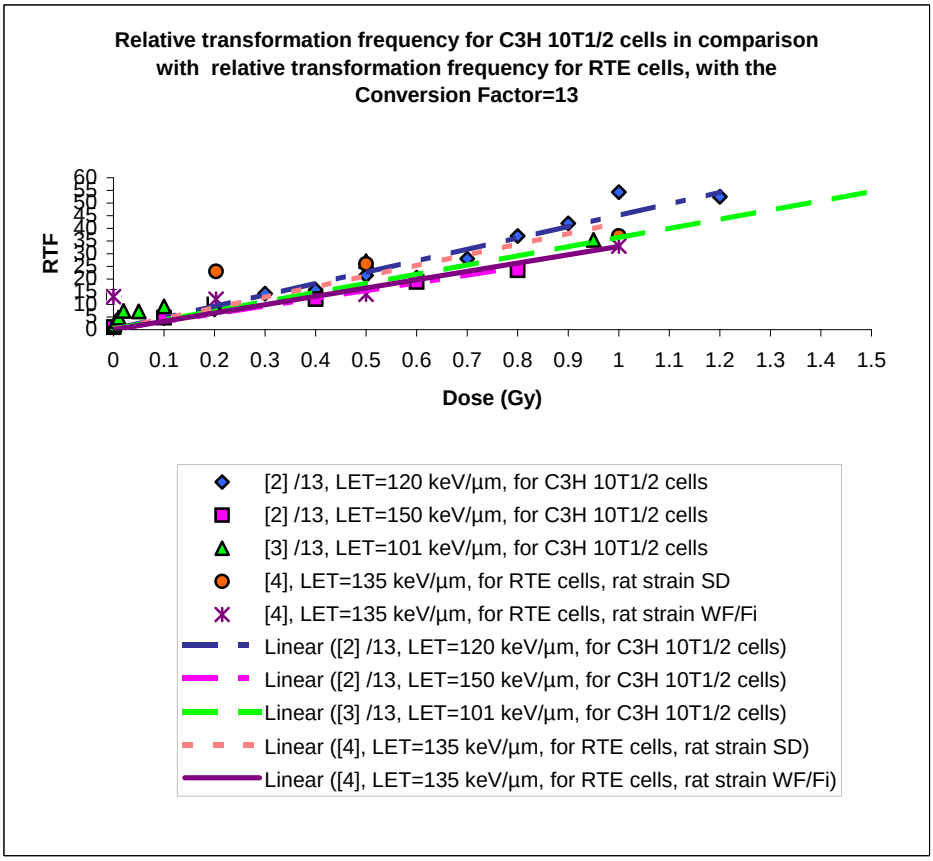

The conclusions that can be drawn from this graph are:

- if we multiply the data for RTE cells by a factor of 13, we can obtain almost the same data as for C3H 10T1/2 cells, i.e. the same slope of the dose-response function;

- there is a significant difference between the RTF for the two rat strains, in the same dose interval, i.e. α-irradiation is more efficient to induce cell transformation in the SD cells than in the WF/Fi cells.

After studying the Cell Surviving Fraction (CSF), the same results regarding the difference between the two rat strains were obtained: WF/Fi rat cells were 1.7 times more radiosensitive than SD rat cells. This difference in sensitivity to α-particle irradiation might be a reflection on:

(1) the nature of cell damage induced by high-LET radiation,

(2) the epithelial cell-repair capacity and

(3) other cellular parameters involved in the metabolic capability [4].

While all the data considered until now were on animals, the general interest is on lung cancer risk in humans induced by radon and its progeny. But the effects of radon on rats may be used as an approximation of the effect on humans.

The next major step of the present study was to develop a predictive dose-response model in order to calculate the lung cancer risk induced by radon and its progeny specifically at low doses. Since the role of low dose radon exposure in the occurrence of lung cancer remains largely unclear, lung cancer risk assessment must be based on a model in order to study what would be the situation in the case of domestic exposure. Epidemiological studies of underground miners and experimental animal studies have documented that exposure to high levels of radioactive ^{222}Rn and its decay products can cause lung cancer. Recent comprehensive analyses of lung cancer risk associated with inhalation exposures to radon progeny have been exclusively based on epidemiological studies with underground uranium miners. Current practice is to determine the probability of lung cancer at low environmental exposures and exposure rates, as they are typically encountered in homes, by extrapolating these occupational lung cancer risk estimates to the lower exposure range.

Estimates of radon risk at low doses are typically extrapolated by the linear no-threshold (LNT) model based on studies of lung cancer occurrence in miners. However, Erickson [5], among others, have investigated the possibility that the LNT model may not be applicable for low doses of radon. That is why a model is necessary to see what happens in different situations by varying different parameters.

There are two different approaches for the assessment of lung cancer risk induced by radon and its progeny: a dosimetric approach and an epidemiological approach. The **epidemiological approach** employs a risk model based on the studies of underground miners. In the present study, an epidemiological approach will be presented.

Mechanistic models for radon progeny induced lung cancer risk have been developed, based on radiation mechanisms at the cellular level. Depending on the initiation and/or promotion properties of ionizing radiation, we distinguish between an initiation-promotion model and a promotion model, which may be most efficient

at different exposure levels. Cigarette smoke or other carcinogenic substances may also act as initiators and/or promoters [6]. For the issue of risk from radon progeny exposure, however, we need information about cell killing and transformation in bronchial epithelial cells, exposed *in vivo* to the LET (linear energy transfer) spectrum of radon progeny alpha particles. Thus, in order to utilize the currently available experimental data, we must make a three-fold extrapolation with respect to differences (1) in cell type (fibroblastic cell versus epithelial cell, and primary cell versus immortalized cell), (2) in LET (relatively monodisperse LET in the experiments versus LET spectrum of radon progeny alpha particles in bronchial epithelium), and, (3) in exposure condition (*in vitro* versus *in vivo*) [6]. The first two points have already been discussed above, and the third one will be discussed below.

In vitro assays of oncogenic transformation are usually carried out with the mouse embryo fibroblast cell line C3H 10T1/2. There is no information regarding oncogenic transformation under *in vivo* conditions. Thus, for the time being, it is assumed that the shape of the *in vitro* transformation function, as borne out by the experimental data of Miller et al. [2] and Bettega et al. [3], is the same for *in vivo* exposures, though absolute numbers may be different. Furthermore, cell survival studies for high LET radiations have indicated that cellular survival under *in vivo* conditions is very similar to that obtained under *in vitro* conditions [7].

THE MECHANISTIC MODEL

There are three models, based on the terminology of initiation and promotion: initiation-promotion, promotion and cigarette smoke promotion. From these three models, **the initiation-promotion model** is the one that will be more thoroughly presented in this paper.

We will consider the case in which cells are initiated and promoted by radiation. The equation for calculating the risk as a function of dose, in this case, is:

$$R(D) = C_1 \cdot \alpha \cdot D \cdot \left[\exp(-\gamma D)\right] \cdot C_2 \cdot \left\{\lambda_1 + \lambda_2 \cdot p \cdot \left[1 - \exp(-\gamma D)\right]\right\}^n$$

where: R(D) is the risk as a function of dose;

$C_1 \cdot \alpha \cdot D \cdot \left[\exp(-\gamma D)\right]$ represents the initiation term and

$C_2 \cdot \left\{\lambda_1 + \lambda_2 \cdot p \cdot \left[1 - \exp(-\gamma D)\right]\right\}^n$ represents the promotion term;

we assume $C_1 \cdot \alpha \cdot C_2 = 1$ and n = 1;

γ represents the cell killing, $\gamma = \frac{1}{D_0}$;

λ_1 and λ_2 are mitotic rates, and

p is the effectiveness of stimulated cellular division.

Normally, a cell has a mitotic rate λ_1 which may increase to λ_2, the rate of division under conditions of tissue replacement. For the lung, a slowly dividing tissue, we may take $\lambda_1 = 0.033$ if we take the cell cycle of 30 days [8], or $\lambda_1 = 0.01$ d^{-1}, if we consider the cell cycle of 100 days, and $\lambda_2 = 1$ d^{-1}. The best fit to the epidemiological data is achieved for a value of n = 1, which has been adopted in all previous simulations.

The parameter p denotes the probability that a progenitor cell must divide as a direct result of the death of an epithelial cell or describes the effectiveness of stimulated cellular division, caused by local cell killing, relative to the normal mitotic activity of lung tissue. For secretory cells we may let p = 1, and for basal cells this probability may be much smaller due to the sequential differentiation required to yield epithelial cells. The value of p = 1 means that each killed epithelial cell will force a stem cell to divide, while values smaller than 1 indicate the existence of a multistage renewal system.

So, the simplest form of the equation for R(D) is:

$$R(D) = D \cdot [\exp(-\gamma D)] \cdot \{\lambda_1 + \lambda_2 \cdot p \cdot [1 - \exp(-\gamma D)]\}$$

A) For a comparison of our theoretical predictions with available epidemiological information, the data on relative lung cancer risk in the U.S. Colorado Plateau uranium miners reported by Hornung and Meinhardt [9] have been chosen. As the cumulative exposure was expressed in WLM in Hornung and Meinhardt's article, the transformation of dose values in Gy was necessary, using a conversion factor (CF) equal, for the beginning, to 5. This means that 1 WLM = 0.005 Gy.

To study the effect of different parameter combinations on the risk function, including the promotional term, for the WF/Fi rat strain (γ = 1.298 Gy^{-1}), only one parameter was varied at a time while keeping the other ones constant in order to see which one could change the result in a significant way.

First of all, we tried to see which value of the exposure-dose conversion factor CF (CF = 5, 6 or 7) gives the closest results to the epidemiological data. The results obtained suggested that the best value for the conversion factor was CF = 7. This value provided the best fit to the epidemiological data for doses higher than 15 Gy. For smaller dose values, the variation of CF does not appreciably change the results.

B) The second parameter variation deals with changing the value of p (the effectiveness of promotion). We used p = 1, 0.25, and 0.05. The conclusion that we could draw after many calculations was that the variation of the promotion by cell killing does not affect very much the results, although the best results, i.e. closest to the epidemiological data, were obtained for p = 0.05 (considering again the case with promotion).

C) The other important parameter that we were interested in was the mitotic rate λ_1. In the first case, it had the value 0.033 (equivalent to a cell cycle of 30 days), but we wanted to see what happens if we take a cellular cycle of 100 days, so λ_1=0.01, by keeping the other parameter values constant (CF = 5, p = 1, etc.).

In order to find out which is the importance of the mitotic rate (respectively the cell cycle duration) in the assessment of lung cancer risk, both values: 0.033 and 0.01 (for 30, respectively 100 days) were considered and compared for the case with the promotion term, for the WF/Fi rat strain.

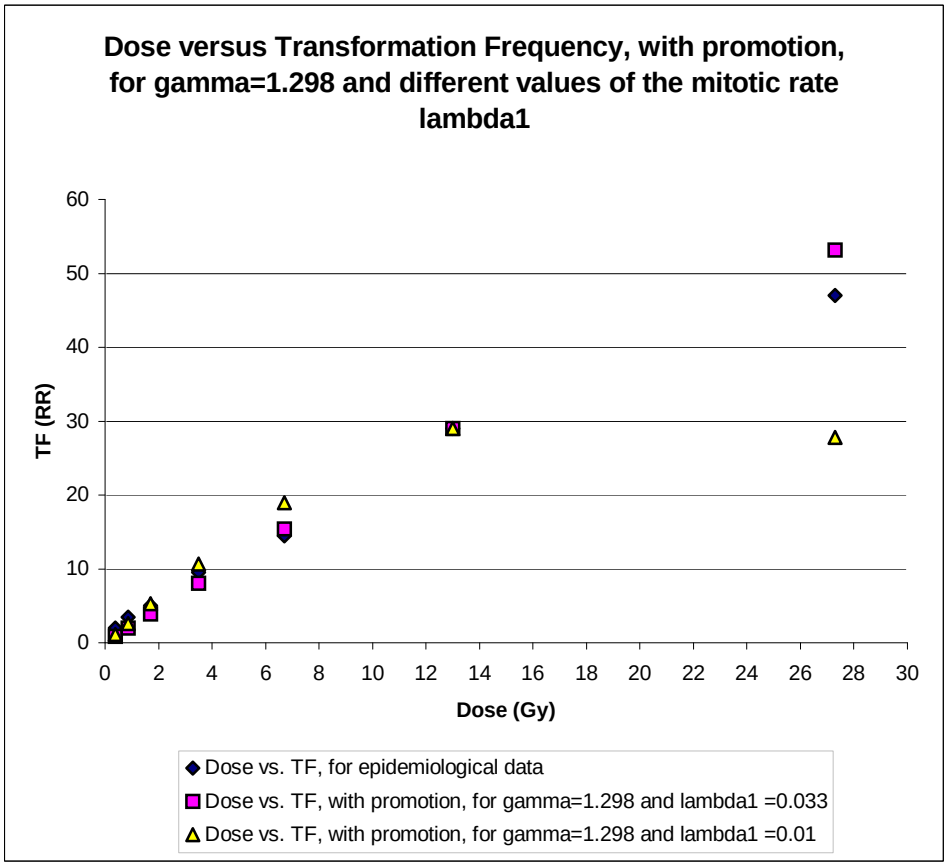

From this graph, one can clearly see that there is a great difference between the case where we considered the cell cycle equal to 100 days (λ_1 = 0.01d^{-1}) and the one in which we considered the cell cycle equal to 30 days (λ_1 = 0.033 d^{-1}) for doses higher than 15 Gy, so for cumulative exposures higher than 2600 WLM, while for doses under 15 Gy, the data almost coincide with the epidemiological data. This phenomenon of risk decreasing with increasing dose rate for high cumulative exposures is commonly called the “inverse dose-rate effect”.

CONCLUSIONS

The initiation-promotion model proposed in this paper provides estimates of the lung cancer risk induced by radon and its progeny and estimates of the resulting changes in the risk from different variations of the following parameters: dose-exposure conversion factor, effectiveness of promotion by cell killing, mitotic rate, rat strain, etc.

The results obtained with this model suggest that with different combinations of parameter values, we can predict lung cancer risk functions, which are in a good agreement with the epidemiological data. For the same case considered (with the promotion term and for the WF/Fi rat strain), the closest fits to the epidemiological data were obtained for CF = 7, p = 0.05 and $\lambda_1 = 0.033\ d^{-1}$. Within the error bars of the epidemiological data, the variation of the conversion factor and promotion effectiveness does not change very much the results for high doses. For doses lower than 15 Gy, for all the variations of CF, p and λ_1, the calculated risk almost coincides with the epidemiological data reported by Hornung and Meinhardt for Colorado Plateau uranium miners.

The most important factor is the variation of the mitotic rate λ_1. For doses higher than 15 Gy (which means for cumulative exposure over 2600 WLM), i.e. in the domain of high cumulative exposures, the predicted lung cancer risk is higher for a cell cycle of 30 days than for 100 days. In other words, carcinogenic risk increases with decreasing dose rate. This phenomenon can be explained by the "inverse dose-rate effect", an effect that occurs only at sufficiently high doses, while for low doses, the classical "dose-rate effect" seems to dominate.

REFERENCES

1. *J. H. Lubin et al*: "Radon and lung cancer risk: a joint analysis of 11 underground miners studies", U. I. Department of Health and Human Services, NIH Publication No. 94-3644 (1994);
2. *R. C. Miller et al*.: "The biological effectiveness of radon-progeny alpha particles. II Oncogenic transformation as a function of linear energy transfer", Radiation Research 142, 54-60 (1995);
3. *D. Bettega, P. Calzolari, G. N. Chiorda, L. Tallone-Lombardi* : "Transformation of C3H 10T1/2 cells with 4.3 MeV α particles at low doses: effects of single and fractionated doses", Radiation Research 131, 66-71 (1992);
4. *J. L. Poncy, C. Kugel, F. Tourdes, I. Bailly*: "In vitro radiation-induced effects on rat trachel epithelial cells I and II", Laboratoire de Radio Toxicologie, France;
5. *B. Erickson*: "Low dose radon as alternative therapy for chronic illness", WONUC Conference on the Effects of Low Doses of Ionizing Radiation on Health, Versailles (1999);
6. *W. Hofmann, D. J. Crawford-Brown, M. G. Menache*: "Mechanistic models for radon-induced lung cancer risk based on cellular radiation effects", Salzburg (1993);
7. *M. Mebust, D. J. Crawford-Brown, W. Hofmann, H. Schöllnberger*: "Testing extrapolation of a biologically based exposure-response model from *in vitro* to *in vivo* conditions", Regulatory Toxicology and Pharmacology 35, 72-79 (2002);
8. *Committee on Health Risks of Exposure to Radon*: "Health effects of exposure to radon" (Beir VI), National Academy Press, Washington, P.C. (1999);
9. *R. W. Hornung, Th. J. Meinhardt*: "Quantitative risk assessment of lung cancer in U.S. uranium miners", Health Physics, Vol. 52, No. 4 (1987);

10. *W. Hofmann, D. J. Crawford-Brown, W. Zhao, M. C. Menache*: "Predictive dose-response models for the assessment of radon-induced lung cancer risk: cellular radiation effects", Salzburg (1993);
11. *L. Tomášek, S. C. Darby, Th. Fearn, A. J. Swerdlow, V. Plaček, E. Hunz*: "Patterns of lung cancer mortality among uranium miners in West Bohemia with varying rates of exposure to radon and its progeny", Radiation Research 137, 251-261 (1994);
12. *F. T. Cross, G. E. Dogle, R. A. Gies, L, G. Smith, R. L. Buschbom*: "Experimental animal studies of radon and cigarette smoke", Washington;
13. *C. Cosma, T. Jurcut*: "Radonul si mediul inconjurator", Ed. Dacia, Cluj-Napoca, (1996);
14. *G. Monchaux*: "Contribution of animal experimental data for the risk assessment of exposure to radon decay products", Institut de Protection et du Sũretė Nuclėaire, France;
15. *W. Hofmann, M. G. Mėnache, D. J. Crawford-Brown, R. S. Carwell, L. R. Karam*: "Modeling energy deposition and cellular radiation effects in human bronchial epithelium by radon progeny alpha particles", Health Physics, Vol. 78, No. 4 (2000);
16. *D. J. Crawford-Brown*: "Modeling the modification of the risk of radon-induced lung cancer by environmental tobacco smoke", Risk Analysis, Vol. 12, No. 4 (1992).